Fritz-Haber-Institut der Max Planck Gesellschaft
Technische Universiät Berlin

Institut für Theoretische Physik

Fakultät II

Master Thesis

First-principle Study of Thermoelectric Magnesium Silicides with High-Throughput Techniques

Hagen-Henrik Kowalski

Matriculation Number: 333306

07.10.2016

Superviser

Prof. Dr. Andreas Knorr Second Supervisor

Prof. Dr. Matthias Scheffler

0.1 Abstract

Heat transport and thermal conductivities are of pivotal importance in many scientific and technological applications, e.g., in thermoelectric compounds. These materials could play a key role to establish an ecologic and sustainable energy economy, given that they allow to recover otherwise wasted heat and transform it into useful voltage. The search for a thermoelectric material that is efficient enough to enable an economically viable, large scale deployment of such thermoelectric "waste heat recovery" devices is, however, still ongoing. Over the last decade, the development of

ab initio theories of heat transport have enabled critical insights in this field. Nonetheless, a first-principles assessment of heat transport remains computationally expensive, thus preventing a systematic *ab initio* high-throughput search for efficient thermoelectric materials across compositional and structural space. To overcome this hurdle, many semi-empirical approximations have been proposed and employed in literature. In this work, the validity and applicability of these techniques are specifically scrutinized using magnesium silicide (Mg_2Si) as an example. After critically reviewing the performance of first-principle techniques for the computation of the thermodynamic equilibrium and non-equilibrium (heat transport) of this material, we compare these *ab initio* results to simpler, semi-empirical approaches. Subsequently, we investigate to which extent these approaches are transferable, i.e., if they can be applied to doped Mg_2Si as well. These studies reveal that the typically used semi-empirical approaches for heat transport modeling are indeed capable to predict qualitative trends, e.g., that the thermal conductivity decreases by doping. However, no reliable quantitative predictions are possible. Eventually, we present a technique that allows to overcome this limitation: In contrast to all the previous approximations, this approach is parameter-free, since all required ingredients are extracted from quasi-harmonic first-principles calculations. We demonstrate the potential in a proof-of-concept study and discuss which computational bottlenecks in the implementation need to be overcome to make this technique generally applicable.

0.2 Zusammenfassung

Wärmetransport und die thermische Leifähigkeit sind von zentraler Bedeutung in sowohl wissenschaftlichen als auch technischen Anwednungen, als Beispiel hierbei seien thermoelektrische Materialien genannt. Solche Materialen könnten in der Zukunft eine entscheidende Rolle in einer ökologischen und nachhaltigen Energiewirtschaft spielen, da sie es ermöglichen, Elektrizität aus Abärme zu gewinnen. Bisher wurde jedoch kein thermoelektrisches Material gefunden, das solch eine Stromgewinnung aus Abwärme wirtschaftlich intressant macht. Über die letzten zehn Jahre haben Fortschritte im Bereich der *ab-initio* Theorie des Wärmetransports tiefe Einsichten in das Feld gewhärt. Nichtsdestotrotz bleiben *ab-initio* Rechnungen zur Bestimmung des Wärmetransports extrem rechenintesiv, weshalb solche Rechnung auf grossen Skalen nicht möglich sind. Um dennoch aussagen über möglichst viele Materialen treffen zu können wurden mehrere semi-empirische Methoden entwickelt. In dieser Arbeit wurde am Beispiel Mg_2Si die Güte und Anwendbarkeit solcher Methoden untersucht. Nach einer kritischen Auseinandersetzung mit existierenden *ab initio* Techniken zur Bestimmung des thermischen Gleich- und nicht Gleichgewichts von Mg_2Si vergleichen wir die Resultate der *ab-initio* Rechnungen mit simpleren, semi-empirischen Modellen. Anschliessend untersuchen wir, wie und ob diese Methoden auch auf *gedoptes* Mg_2Si angewendet werden können. Dabei stellt sich heraus, dass die gängigen semi-empirischen Modelle zum Wärmetransport durchaus in der Lage sind qualitativ richtige Trends, zum Beispiel das Senken der thermischen Leitfähigkeit durch *Doping*, wiederzugeben. Allerdings sind dabei keine verlässlichen vorhersagen möglich. Schlussendlich präsentieren wir eine Technik mit der es möglich ist diese Einschänkungen zu überkommen. Anders als alle Methoden, die davor besprochen werden, ist unser Ansatz frei von jeglichen zu bestimmenden Parametern, da alle benötigten Daten aus quasi-harmonischen *ab-initio*-Rechnungen gewonnen werden können. Das Potential dieser Methode wird in einer *proof-of-concept*-Studie demonstriert. Desweiteren diskutieren wir, welche rechentechnischen Limitationen bei der Implementation überwunden werden müssen.

Contents

Contents

1 Introduction

Heat transport and thermal conductivities are of pivotal importance in many scientific and technological applications: On the one hand, boosting heat transport at the nanoscale is a critical issue in th CPU design todate, since local "hot spots" can critically affect the lifetime of semiconducting devices. On the other hand, suppressing heat transport is also a critial issues in the design of so called "thermal barrier coatings" for airplane turbines [1]. These coatings, which feature a minute thermal conductivity already, protect the underlying alloys from the high temperatures generated during combustion. This allows to increase the operational temperature and thus also the fuel efficiency of the turbine. Last but not least, tailoring the thermal conductivity is also crucial for the development of thermoelectric materials, which in principle allow to recover otherwise wasted heat and transform it into useful voltage. The efficiency of this transformation can be characterized by the thermoelectric figure of merit

$$ZT = \frac{\sigma S^2 T}{\kappa_{electron} + \kappa_{phonon}}, \tag{1.1}$$

with T being the temperature, σ the electrical conductivity, S the Seebeck coefficient, and $\kappa_{electron}$ and κ_{phonon} the contributions to the thermal conductivity of electrons and phonons, respectively. So far, the use of thermoelectric materials to convert waste heat into electricity is limited to very few applications: For example, space probes such as the Voyager I and II make use of thermoelectric elements to produce electricity. Increasing ZT and thus the efficiency would allow their application also in other fields, e.g., to harvest wast heat in automotive thermoelectric generators [2] or in industrial plants. For this reason, thermoelectric materials are regarded as a promising technology to establish an ecologic and sustainable energy economy.

One possible strategy to increase ZT is to introduce defects and/or dopants into the material [44], which in turn lowers the lattice thermal conductivity κ_{phonon}. Over the last decade, the development of *ab initio* theories that allow to compute of κ_{phonon} from first principles have enabled critical insights in this field: Most of these techniques rely on the linearized Boltzmann transport equation, which can be solved either directly [37, 26] or in the single mode relaxation time approximation [26]. Other techniques rely on *ab initio* molecular dynamics simulations to sample the nuclear motion; the thermal conductivity can then for instance be determined via the Green-Kubo formalism [29]. All of this techniques come, however, at a considerable computational cost: Effectively, this prevents a systematic *ab*

initio high-throughput search for efficient thermoelectric materials across compositional and structural space, especially for the more complex material classes. Often, this computational hurdle is circumvented by applying a semi-empirical approximation [41, 40] in the modeling of the heat transport. A variety of such approximations exists, but their accuracy is still topic of scientific debate.

In this thesis, the validity and applicability of these semi-empirical approximations is scrutinized using magnesium silicide (Mg_2Si) as an example: First, a concise introduction to the fundamental physical concepts used in this thesis is given in Sec. 2. This includes an introduction to electronic-structure theory and to the theoretical foundation of heat transport calculations. In Sec. 3, the properties of magnesium silicide (Mg_2Si) are investigated and critically discussed with respect to the employed approximations. In particular, these calculations are used to illustrate the practical aspects of the employed computational techniques. Particular focus is laid on the harmonic and anharmonic vibrational properties that determine heat transport. To better frame the discussion, Mg_2Si is systematically compared with silicon (diamond structure) and CuCl (zincblend structure), two materials known for their particularly harmonic/anharmonic character. Eventually, these first-principle calculations for Mg_2Si are systematically compared against the outcome of computations that make us of simpler, semi-empirical approximations and parameters to model heat transport. This lays the founding for Sec. 4, in which the influence of doping on the (vibrational transport) properties of Mg_2Si are discussed in detail. Last but not least, the outlook in Sec. 5 introduces and discusses a technique that allows to overcome the limitations of the previously discussed approximations. The potential of this technique is demonstrated in a proof-of-concept study.

2 Theory

The fundamental equation describing the quantum mechanical behavior of N_{el} electrons $(\mathbf{r} = \mathbf{r}_1, \cdots, \mathbf{r}_{N_{el}})$ and N nuclei $(\mathbf{R} = \mathbf{R}_1 \cdots \mathbf{R}_N)$ in any non-relativistic material is the Schrödinger Equation

$$H(\mathbf{r}, \mathbf{R})\Psi(\mathbf{r}, \mathbf{R}) = E\Psi(\mathbf{r}, \mathbf{R}). \tag{2.1}$$

Here, $\Psi(\mathbf{r}, \mathbf{R})$ is the many-body wavefunction of the combined electronic-nuclear systems, $E(\mathbf{r}, \mathbf{R})$ is its energy, and $H(\mathbf{r}, \mathbf{R})$ is the Hamiltonian that describes the interaction of the nuclei and the electrons [3]:

$$H(\mathbf{r}, \mathbf{R}) = T_{el} + T_{nuc} + V_{el-nuc}(\mathbf{r}, \mathbf{R}) + V_{el-el}(\mathbf{r}) + V_{nuc-nuc}(\mathbf{r}, \mathbf{R}) \,. \tag{2.2}$$

T_{el} and T_{nuc} are the kinetic energies of the electrons and the nuclei. With m_e and M_I being the respective masses, they can be expressed in real space as

$$T_{el} = -\frac{1}{2}\sum_i \frac{\nabla_{\mathbf{r}_I}^2}{m_e} \quad \text{and} \quad T_{nuc} = -\frac{1}{2}\sum_I \frac{\nabla_{\mathbf{R}_I}^2}{M_I} \,. \tag{2.3}$$

The potentials $V_{el-nuc}(\mathbf{r}, \mathbf{R})$, $V_{el-el}(\mathbf{r})$, and $V_{nuc-nuc}(\mathbf{R})$ describe the electrostatic electron-nuclei, electron-electron, and nuclei-nuclei interaction and are given in realspace by

$$V_{el-nuc}(\mathbf{r}, \mathbf{R}) = -\sum_{i,I} \frac{Z_I}{|\mathbf{r}_i - \mathbf{R}_I|} \tag{2.4}$$

$$V_{el-el}(\mathbf{r}) = \frac{1}{2}\sum_{i,j} \frac{1}{|\mathbf{r}_i - \mathbf{r}_j|} \tag{2.5}$$

$$V_{nuc-nuc}(\mathbf{R}) = \frac{1}{2}\sum_{I,J} \frac{Z_I Z_J}{|\mathbf{R}_I - \mathbf{R}_J|} \,. \tag{2.6}$$

Here, $\mathbf{r}_i$ denotes the position of the ith electron and $\mathbf{R}_I$ the one of the Ith nucleus with charge Z_I. The function $\Psi(\mathbf{r}, \mathbf{R})$ that solves Eq. (2.1) fully characterizes the combined electronic-nuclear systems. Its numerical solution is, however, a formidable problem due to the inherent coupling of fast (electron) and slow (nuclei) degrees of freedom. Despite some notable exceptions [48, 49, 52, 53], it is safe to assume that the dynamics of the electrons and the nuclei occurs on different timescales, given that the nuclear mass is much larger than the one of the electrons $(M_I \gg m_e)$. This so called Born-Oppenheimer approximation [3] implies that the electrons adapt to every movement of the nucleus instaneously, which allows to treat

the electronic $\Psi_{el}(\mathbf{r}, \{\mathbf{R}\})$ and the nuclear system $\Psi_{nuc}(\mathbf{R})$ consecutively by approximating the full state in a product ansatz $\Psi(\mathbf{r}, \mathbf{R}) = \Psi_{el}(\mathbf{r}, \{\mathbf{R}\})\Psi_{nuc}(\mathbf{R})$. The chosen notation $\{\}$ highlights that the nuclei enter the electronic wavefunction $\Psi_{el}(\mathbf{r}, \{\mathbf{R}\})$ only parametrically. Accordingly, one gets one electronic Schrödinger equation

$$\underbrace{(T_{el} + V_{el-nuc}(\mathbf{r}, \{\mathbf{R}\}) + V_{el-el}(\mathbf{r}))}_{H_{el}} \Psi_{el}(\mathbf{r}, \{\mathbf{R}\}) = E_{el}(\{\mathbf{R}\})\Psi_{el}(\mathbf{r}, \{\mathbf{R}\}) . \qquad (2.7)$$

In turn, the energy of the electronic system $E_{el}(\{\mathbf{R}\})$ determines the potential for the nuclear Schrödinger equation:

$$\underbrace{(T_{nuc} + V_{nuc-nuc}(\mathbf{R}) + E_{el}(\{\mathbf{R}\}))}_{H_{nuc}} \Psi_{nuc}(\mathbf{R}) = E_{nuc}\Psi_{nuc}(\mathbf{R}) . \qquad (2.8)$$

Numerical approaches to solve these equations are discussed in the following sections (electrons: Sec. 2.1; nuclei: Sec. 2.2)

2.1 Density-functional Theory

In spite of the fact that the Born-Oppenheimer approximation discussed above reduces the complexity of the problem immensely, solving the electronic Schödinger equation (2.7) still constitutes a formidable problem, given that the solution depends on the $3N_{el}$ electronic degrees of freedom. Various so called wavefunction-based algorithms and techniques have been developed over the last decades to tackle this problem [4]; discussing them would however go beyond the scope of this thesis. Rather, we will focus on the *ab initio* technique used in the later sections of this work, i.e., density-functional theory (DFT), for the formulation of which Walther Kohn was awarded the Nobel prize in 1998. In this formalism, the electronic ground state of a system is fully described by the respective electronic density

$$n(\mathbf{r}) = N_{el} \int |\Psi(\mathbf{r}, \mathbf{r}_2, ..., \mathbf{r}_{N_{el}})|^2 d\mathbf{r}_2...d\mathbf{r}_{N_{el}} , \qquad (2.9)$$

which only depends on three cartesian coordinates. Formally, this massively reduces the complexity of the problem.

The essence of DFT is captured in the two Hohenberg-Kohn theorems [5]:

Theorem 1 (First HK-Theorem) *For any system of interacting particles in an external potential exists a bijection between the density and the external potential.*

Theorem 2 (Second HK-Theorem) *A functional $E_{el}[n]$ of the density exists, the density which minimizes this functional is the ground state density, and the minimum of this functional is the ground state energy.*

The functional $E_{el}[n]$ can be written as:

$$E_{el}[n] = E_{ext}[n] + F[n] \, . \tag{2.10}$$

Here, $F[n]$ is the functional that contains all interactions between the electrons as well as their kinetic energy and $E_{ext}[n]$ is the interaction energy with an external potential. In our specific case, it is given by V_{el-nuc} of Eq. (2.6)

$$E_{ext}[n] = \int v_{ext}(\mathbf{r})n(\mathbf{r})d\mathbf{r} = -\sum_I \int \frac{Z_I\, n(\mathbf{r})}{|\mathbf{r} - \mathbf{R}_I|}d\mathbf{r} \, . \tag{2.11}$$

Although formally exact, DFT is not particularly useful in this formulation, given that no closed analytical expression for $F[n]$ has been found so far. Furthermore, also approximative formulations of $F[n]$ have not yet been able to reach a satisfactory accuracy [8]. As discussed in the next section, these problems can be partially circumvented in the *Kohn-Sham formalism* [7]. This, however, requires to drop the fomally appealing description in terms of an electron density and to reintroduce individual electronic states.

2.1.1 Kohn-Sham Formalism

The crucial point in the *Kohn-Sham formalism* [7] is the introduction of a supplementary, **non-interacting** electronic system that can be described by single-particle states $\tilde{\psi}_1(\mathbf{r}), \cdots, \tilde{\psi}_{N_{el}}(\mathbf{r})$. Such a system exhibits the electronic density

$$\tilde{n}(\mathbf{r}) = \sum_i^{N_{el}} \int |\tilde{\psi}_i(\mathbf{r})|^2 d\mathbf{r} \, ; \tag{2.12}$$

the total energy functional in Eq. (2.10) simplifies to

$$\tilde{E}_{el}[\tilde{n}] = E_{ext}[\tilde{n}] + \tilde{T}_s[\tilde{n}] \, . \tag{2.13}$$

This only includes the external potential $E_{ext}[\tilde{n}]$, already defined in Eq. (2.11), and the kinetic energy of the **non-interacting** electronic system $\tilde{T}_s$ discussed in more detail below. The variational minimum of this functional is the ground state energy of the non-interacting system and the corresponding density is the one of the ground state. The variational differential is given by:

$$\delta \left(\tilde{E}_{el}[\tilde{n}] - \mu \left[\int \tilde{n}(\mathbf{r})d^3r - N_e \right] \right) = 0 \tag{2.14}$$

A Lagrange parameter μ was introduced to keep the number of particles fixed. This yields the following equation:

$$\frac{\delta T_s[\tilde{n}]}{\delta n} + v_{ext} = 0 \, . \tag{2.15}$$

Solving this equation would require to find an expression for the functional derivative $\delta T_s[\tilde{n}]/\delta n$, first. However, this can be circumvented by reintroducing the single-particle representation, given that for this particular system the kinetic energy is determined by the operator

$$\tilde{T}_s = -\frac{1}{2}\sum_i^{N_{el}} \nabla_i^2 \; . \tag{2.16}$$

The associated Schrödinger equation

$$(-\frac{1}{2}\nabla^2 + v_{ext}(\mathbf{r}))\tilde{\psi}_i(\mathbf{r}) = \epsilon_i \tilde{\psi}_i(\mathbf{r}) \tag{2.17}$$

can be solved at a reasonable computational cost, given that the individual electron can be treated independently.

To find a mapping between the system of interacting electrons and the non-interacting system discussed above, the total energy functional $E_{el}[n]$ for the interacting system (2.10) is rewritten as:

$$E_{el}[n] = E_{ext}[n] + \tilde{T}_s[n] + E_H[n] + \underbrace{\left(F[n] - \tilde{T}_s[n] - E_H[n] \right)}_{E_{xc}[n]} . \tag{2.18}$$

Beside the external potential $E_{ext}[n]$ already defined in Eq. (2.11), this expression includes the electrostatic Hartree energy $E_H[n]$ describing the electronic mean-field repulsion

$$E_H[n] = \frac{1}{2} \int \frac{n(\mathbf{r})n(\hat{\mathbf{r}})}{|\mathbf{r} - \hat{\mathbf{r}}|} d\mathbf{r} d\hat{\mathbf{r}} \tag{2.19}$$

and the kinetic energy $\tilde{T}_s$ of a **non-interacting** electronic system that is required [1] to exhibit the exact same density as the interacting systems that is sought after:

$$n(\mathbf{r}) \overset{!}{=} \tilde{n}(\mathbf{r}) = \sum_i^{N_{el}} \int |\tilde{\psi}_i(\mathbf{r})|^2 d\mathbf{r} \; . \tag{2.20}$$

Eventually, the exchange-correlation (XC) energy $E_{xc}[n]$ subsumes all many-body effects, i.e., the non-classical kinetic energy and the non-classical electron-electron interaction. Minimizing this functional with respect to the density yields the following expression:

$$\frac{\delta \tilde{T}_s[n]}{\delta n} + \underbrace{v_{ext} + v_H + v_{xc}}_{v_{eff}(\mathbf{r})} = 0 \; , \tag{2.21}$$

which takes the exact same form as the respective equation for a non-interacting system (2.15). By this means, we have found a mapping between the equation governing an interacting system in an external potential v_{ext} and the one of a non-interacting system in a different potential v_{eff}. Accordingly, also **non-interacting** problem can be

---

[1]A detailed discussion of this so called *v-representability* requirement and its validity can be found in Ref. [6].

solved by finding the solution of single-particle, **non-interacting** Schrödinger equation

$$\underbrace{\left(-\frac{1}{2}\nabla^2 + v_{eff}(\mathbf{r})\right)}_{h_{KS}} \psi_i(\mathbf{r}) = \epsilon_i \psi_i(\mathbf{r}). \tag{2.22}$$

This equation is called the Kohn-Sham (KS) equation [7]. Again, it can be solved to determine the ground state density $n(\mathbf{r})$ within reasonable computational effort. In contrast to Eq. (2.17), however, the density itself enters $v_{eff}(\mathbf{r})$, so that a *self-consistent field* approach is typically used in practical calculations: Starting from an (educated) initial guess for the density $n^{(0)}(\mathbf{r})$, the electronic energy (see below) is minimized in i iterations by refining the density $n^{(i)}(\mathbf{r})$ until self-consistence is numerically achieved up to a user-defined parameter ϵ, e.g., $\int |n^{(i)}(\mathbf{r}) - n^{(i+1)}(\mathbf{r})| d\mathbf{r} < \epsilon$. Please note that the electronic energy of the interacting systems is

$$E_{el}[n] = \sum_i^{occ} \epsilon_i - E_H[n] - \int v_{xc}[n]n(r)dr^3 + E_{xc}[n] . \tag{2.23}$$

For the ground state density, this yields the potential energy surface for the nuclei:

$$E_{tot} = E_{el}[n] + E_{nuc} . \tag{2.24}$$

2.1.2 Approximative Exchange-Correlation Functionals

In principle, the previously introduced Kohn-Sham formalism provides a practical route to calculate the (exact) electronic ground state. However, a closed analytical form for the thereto required XC functional $E_{xc}[n]$ is not known, so that approximative XC functionals have to be used in practical calculations instead. Different flavours with different levels of accuracy and computational cost exist: Here, we limit ourselves to introduce the concepts behind the approximations used for the calculations in this thesis; the influence of the approximations on the actual computational results are discussed for the practical example of Mg_2Si of interest in this work in Sec. 3

The Local Density Approximation (LDA): In this very common approximation, the XC energy density $\epsilon_{xc}[n]$ at each point in space $\mathbf{r}$ is approximated by the value of the respective XC energy density $\epsilon_{xc}^{LDA}[n]$ that a homogeneous electron gas (jellium model) would exhibit at that density $n(\mathbf{r})$:

$$E_{xc} = \int n(\mathbf{r})\epsilon_{exc}^{LDA}(n(\mathbf{r}))d\mathbf{r} . \tag{2.25}$$

The Generalized Gradient Approximation (GGA): In the spirit of a Taylor expansion, GGA XC functionals do not only take into account the local value of the density $n(\mathbf{r})$,

but also its gradient $\nabla_{\mathbf{r}} n(\mathbf{r})$. Formally, this is achieved by introducing an enhancement factor $F_{xc}[n(\mathbf{r}), \nabla_{\mathbf{r}} n(\mathbf{r})]$:

$$E_{xc} = \int n(\mathbf{r}) \epsilon_{xc}^{LDA}(n(\mathbf{r})) F_{xc}(n(\mathbf{r}), \nabla_{\mathbf{r}} n(\mathbf{r})) d\mathbf{r} \ . \tag{2.26}$$

Due to the fact that some freedom exists in the definition of $F_{xc}(n(\mathbf{r}), \nabla_{\mathbf{r}} n(\mathbf{r}))$, many different flavours of GGAs exist: Some, like the PBE functional [9] and its adaption for solid materials (PBEsol [10]) are formulated to fulfill fundamental properties that the exact XC functional is known to fulfill. Others, like BLYP are specifically constructed to reproduce experimental data.

Hybrid XC Functionals: Both LDA and GGAs suffer from a spurious self-interaction that results into the erroneous tendency of electrons to delocalize [11]. In part, this can be corrected for [12] by replacing a fraction of the GGA exchange with the exact (Hartee-Fock) exchange

$$E_x^{HF} = -\frac{1}{2} \sum_{i,j}^{N_{el}} \int \frac{\psi_i^*(\mathbf{r}) \psi_j(\mathbf{r}) \psi_j^*(\hat{\mathbf{r}}) \psi_i(\hat{\mathbf{r}})}{\mathbf{r} - \hat{\mathbf{r}}} d\mathbf{r} d\hat{\mathbf{r}} \ . \tag{2.27}$$

Popular examples for such a functionals are the PBE0 functional [12]

$$E_{xc}^{PBE0} = \frac{1}{4} E_x^{HF} + \frac{3}{4} E_x^{PBE} + E_c^{PBE} \tag{2.28}$$

or HSE-type functionals [13], in which the bare Coulomb interaction in Eq. (2.27) is additionally screened.

### 2.1.3 Practical Numerical Solution and Implementation

In this section, we shortly summarize some practical aspects that need to be considered when performing KS calculations.

Solving the KS Equations: To efficiently implement Eq. (2.22) in computer code and exploit fast linear algebra libraries, the eigenfunctions ψ_i of the KS Hamiltonian are approximated in a truncated expansion in terms of basis functions ζ:

$$\psi_i = \sum_j c_{ij} \zeta_j(\mathbf{r}). \tag{2.29}$$

Accordingly, Eq. (2.22) becomes a generalized eigenvalue problem:

$$\sum_i h_{li} c_{ij} = \epsilon_j \sum_i o_{li} c_{ij} \tag{2.30}$$
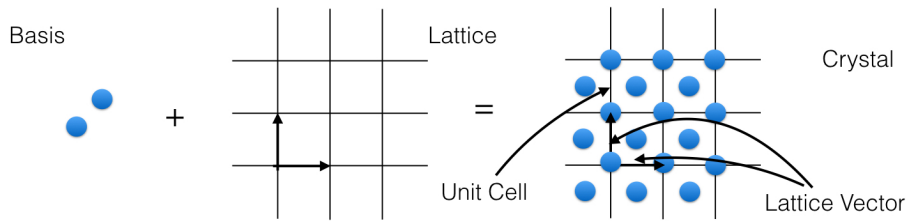
Figure 2.1: Sketch showing how a formally infinite crystal is modeled using periodic boundary conditions starting from a unit cell that contains basis atoms. This unit cell is infinitely repeated in space using the lattice vectors (see text).

With the matrix elements of the kohn-sham hamiltonian h_{ks}

$$h_{li} = \int \zeta_l(\mathbf{r}) h_{ks} \zeta_i(\mathbf{r}) d\mathbf{r} \tag{2.31}$$

and the overlap integral

$$o_{li} = \int \zeta_l(\mathbf{r}) \zeta_i(\mathbf{r}) d\mathbf{r}. \tag{2.32}$$

This approximation, i.e., the convergence of the results of interest with respect to the number of basis functions included, needs to be explicitly investigated to ensure the validity of the results (see Sec. 7).

In this particular work, the all-electron, full potential code *FHI-aims* [33] was used [2], which utilizes atom-centered, numeric orbitals

$$\zeta_j(\mathbf{r}) = \frac{u_{nl}(\mathbf{r} - \mathbf{R}_{at})}{r} Y_{lm}(\Phi, \Theta) \tag{2.33}$$

as basis set. Here $Y_{lm}(\Phi, \Theta)$ are spherical harmonics and $u_{nl}(\mathbf{r} - \mathbf{R}_{at})$ are numerically defined radial functions with $\mathbf{R}_{at}$ being the coordinates of the nucleus to which this specific atomic orbital belongs.

Periodic Boundary Conditions: Obviously, performing DFT calculations for macroscopic materials in a naive approach would be excruciatingly computationally expensive due to the massive number of electron N_{el} that needs to be accounted for. For crystalline materials with translational periodicity, this can be circumvented by applying *periodic coundary conditions*: As sketched in Fig. 2.1, a crystal is thereby described by a finite number of atoms in the primitive unit cell, which is spanned up by the lattice vectors $A = [\mathbf{A}_1, \mathbf{A}_2, \mathbf{A}_3]$. This unit cell is infinitely repeated as described by the translation vector $\mathbf{T}(\mathbf{n}) = A \cdot \mathbf{n}$ with $\mathbf{n} = [n_1, n_2, n_3]$, $n_i \in \mathbb{Z}$.

---

[2]All-electron means that all electrons are treated on the same level. Conversely, pseudo-potential codes only treat the core electrons approximately by effectively including them in a pesudo-potential.

Such a description in terms of periodic boundary conditions imposes restrictions on the wave functions, too. Bloch's theorem states that in this case the wave functions

$$\psi_i(\mathbf{r}, \mathbf{k}) = e^{i\mathbf{k}\cdot\mathbf{r}} u_i(\mathbf{r}) \tag{2.34}$$

can be written as the product of a lattice-periodic function

$$u_i(\mathbf{r}) = u_i(\mathbf{r} + \mathbf{T}(\mathbf{n})) \tag{2.35}$$

and a wavevector $\mathbf{k}$-dependent plane wave. In the case of periodic calculations in *FHI-aims*, this is exploited by using a Bloch-like basis set

$$\chi_j(\mathbf{r}, \mathbf{k}) = \sum_{\mathbf{n}} e^{i\mathbf{k}\cdot\mathbf{T}(\mathbf{n})} \zeta_j(\mathbf{r} - \mathbf{R}_{at} + \mathbf{T}(\mathbf{n})) \tag{2.36}$$

in the expansion in Eq. (2.29). Accordingly, both the KS states and KS Hamiltonian become $\mathbf{k}$-dependent. By this means, one thus formally maps the KS equation for an infinite number of electrons onto the KS equation for the finite number of electrons contained in a unit cell. In turn, however, this problem has to be solved for a formally infinite set of $\mathbf{k}$-vectors. Obviously, only finite $\mathbf{k}$-grid are used in practical calculations. Convergence of the quantities of interest with respect to this numerical parameter needs to be explicitly checked.

2.2 Nuclear Motion

As discussed above, DFT can be used to compute the properties (density, eigenvalues, etc.) and the total energy E_{tot} of the electronic system. The latter determines the potential-energy surface (PES) on which the nuclei move in the Born-Oppenheimer approximation, see Eq. (2.24). Mapping out such a PES for realistic systems, is, however, a formidable problem, given that the dimensionality of the PES scales with the number of degrees of freedom and each single geometric configuration requires an individual self-consistent *ab initio* calculation. Various techniques have thus been developed to efficiently determine properties associated with the nuclei, e.g., optimization algorithms to find the minimum PES (0K equilibrium configuration of the nuclei) or techniques to assess the nuclear dynamics (see Sec. 2.2.1 and 2.2.2). To work efficiently, however, these algorithms require not only the energy of the PES in that particular configurations, but also its derivatives. First order derivatives, i.e., the forces

$$
\begin{aligned}
\mathbf{F}_I &= -\frac{dE_{tot}}{d\mathbf{R}_I} \\
&= -\frac{\partial E_{tot}}{\partial \mathbf{R}_I} - \sum_i \frac{\partial E_{tot}}{\partial \chi_i} \frac{\partial \chi_i}{\partial \mathbf{R}_I} - \sum_{ij} \underbrace{\frac{\partial E_{tot}}{\partial c_{ij}}}_{=0} \frac{\partial c_{ij}}{\partial \mathbf{R}_I} .
\end{aligned} \tag{2.37}
$$

can be expressed analytically within standard DFT: As highlighted by the notation $\partial/\partial\mathbf{R}_I$ for the *partial* derivatives, the first term describes the direct dependence of the total energy on the nuclear degrees of freedom. The second term, the so called *Pulay* term [14], captures the dependence of the total energy on the basis set chosen for the expansion in Eq. (2.33). The last term vanishes, since the ground state total energy constitutes a variational minimum with respect to the expansion coefficients c_{ij}. For higher order derivatives of the total energy, e.g., the Hessian,

$$
\begin{aligned}
\frac{d^2 E_{tot}}{d\mathbf{R}_I d\mathbf{R}_J} &= -\frac{d}{d\mathbf{R}_J}\mathbf{F}_I \\
&= -\frac{\partial\mathbf{F}_I}{\partial\mathbf{R}_J} - \sum_i \frac{\partial\mathbf{F}_I}{\partial\chi_i}\frac{\partial\chi_i}{\partial\mathbf{R}_J} - \sum_{ij} \underbrace{\frac{\partial\mathbf{F}_I}{\partial c_{ij}}}_{\neq 0}\frac{\partial c_{ij}}{\partial\mathbf{R}_J} ,
\end{aligned}
\tag{2.38}
$$

the problem gets more complex, since the forces are *not* variational with respect to the expansion coefficients c_{ij}. Accordingly, a calculation of the Hessian does not only require the analytical derivatives appearing in the first two terms, but also the *response* of the expansion coefficients to a nuclear displacement $\partial c_{ij}/\partial\mathbf{R}_J$. Formally, the $(2n+1)$ theorem [15], i.e., a generalization of Hellman-Feynman theorem [16], shows that knowledge of the n-th order response (i.e. the n-th order total derivative) of the electronic structure with respect to a perturbation is required to determine the respective $(2n+1)$-th total derivatives of the total energy [15]. These response quantities are, however, not directly accessible within DFT: They can be either computed by application of first order perturbation theory [21] or by evaluating the Hessian numerically with finite differences:

$$
\frac{d^2 E_{tot}}{d\mathbf{R}_I d\mathbf{R}_J} \approx -\frac{F_I(\delta\mathbf{R}_J)}{\delta\mathbf{R}_J}
\tag{2.39}
$$

The latter technique has been used in this work; the practical details are discussed in Sec. 2.2.2.

2.2.1 Molecular Dynamics

Molecular dynamics (MD) techniques are the most accurate approach to assess the nuclear dynamics. In this technique, the Schrödinger equation for the nuclei (2.8) is solved numerically in the classical limit [3]. For this purpose, the classical equations of motion

$$
\mathbf{F}_I(t) = M_I\ddot{\mathbf{R}}_I(t)
\tag{2.40}
$$

are stepwise integrated $t \to t + \Delta t$ for a finite timestep Δt starting from a chosen initial condition for the positions $\mathbf{R}_I(t_0)$ and the velocities $\dot{\mathbf{R}}_I(t_0)$. Most prominently, the *Velocity*

---

[3]Due to the large mass of nuclei, quantum-mechanical effects can indeed be often neglected in their dynamics. See Sec. 3.2.2 for a more in-depth discussion of this approximation for the practical example of Mg_2Si.
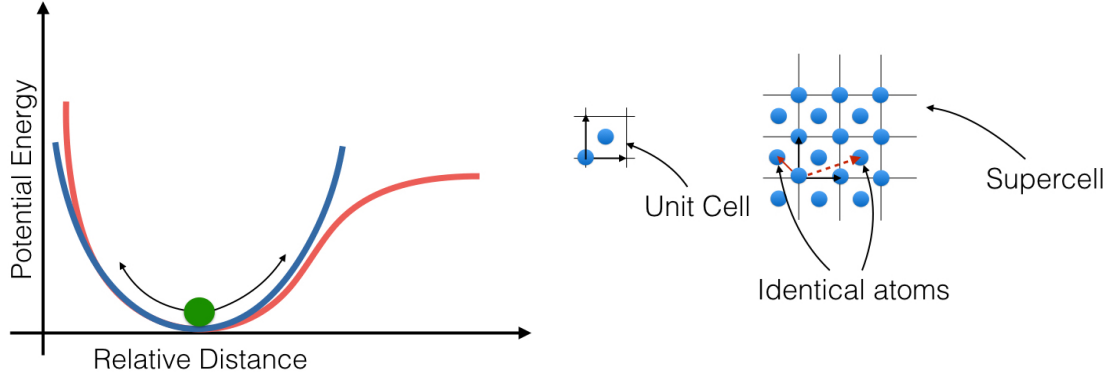
Figure 2.2: Left: Sketch showing a potential energy surface (red) that is approximated in the harmonic approximation (red) around the equilibrium position. Right: Sketch of a supercell, the red arrows mark two periodic images that are connected to the respective primitive atom in the supercell via lattice vectors (see text)

Verlet algorithm [17] is used for this purpose:

$$\mathbf{R}_I(t + \Delta t) = \mathbf{R}_I(t) + \dot{\mathbf{R}}_I(t)\Delta t + \frac{\mathbf{F}_I(t)}{2M_I}\Delta t^2 \qquad (2.41)$$

$$\dot{\mathbf{R}}_I(t + \Delta t) = \dot{\mathbf{R}}_I(t) + \frac{\mathbf{F}_I(t) + \mathbf{F}_I(t + \Delta t)}{2M_I}\Delta t \qquad (2.42)$$

Please note that these equations can be augmented by so called *thermostats* [17] to sample different thermodynamic ensembles. Given that the forces $\mathbf{F}_I(t)$ acting on the nuclei can be computed within DFT following Eq. (2.37), this technique can be directly coupled to DFT calculations to perform so called *ab initio MD* simulations. For long time scales t and large systems, however, such an approach can rapidly become computationally expensive, given that it requires $t/\Delta t$ force evaluations. In the following sections, we will thus discuss approximative techniques that allow to estimate properties stemming from the nuclear dynamics.

2.2.2 The Harmonic Approximation

The harmonic approximation is the most well known and most used technique to describe and interpret the nuclear motion, especially in solid state theory. To start, the PES is approximated by a truncated, second order Taylor expansion around its minimum, i.e., the 0K equilibrium positions $\mathbf{R}^{eq}$ shown in Fig. (2.2).

$$E_{tot}^{ha} \approx E_{tot} + \sum_{I,\alpha} F_I^\alpha u_I^\alpha + \frac{1}{2} \sum_{I,J,\alpha,\beta} \Phi_{IJ}^{\alpha\beta} u_I^\alpha u_J^\beta \; . \qquad (2.43)$$

Here, the $u_I^\alpha = \mathbf{R}_I^\alpha - \mathbf{R}_I^{\alpha,eq}$ are the displacements of the atoms around their equilibrium positions. Please note that the static term E_{tot} is the total energy in equilibrium, the linear

term vanishes due to the fact that the forces F_I^α vanish in equilibrium, but the Hessian (or harmonic force constants)

$$\Phi_{IJ}^{\alpha\beta} \quad = \quad \frac{\partial^2 E_{tot}}{\partial R_I^\alpha \partial R_J^\beta} \tag{2.44}$$

introduced in Eq. (2.43) above do not (see Fig. 2.2). The ansatz

$$u_I^\alpha = \frac{A}{\sqrt{M_I}} \epsilon_I^\alpha(\mathbf{q}, s) e^{i(\mathbf{q}\cdot\mathbf{R}_I - \omega t)} \ , \tag{2.45}$$

the physical interpretation of which is discussed below, separates and solves the equation of motion in this approximate potential. In this context, it is useful to express the index of the I-th atom using periodic boundary conditions as $I \to n\tilde{I}$, where $\tilde{I}$ denotes the $\tilde{I}$-th atom in the primitive unit cell and n denotes that this is its n-th periodic image shifted by a lattice translation vector $\mathbf{T}(n)$ (see Sec. 2.1.3). In this notation, the equations of motion become an eigenvalue problem

$$\mathbf{D}(\mathbf{q})\epsilon(\mathbf{q}) = \omega^2(\mathbf{q})\epsilon(\mathbf{q}) \quad \text{with} \quad D_{\tilde{I}\tilde{J}}^{\alpha\beta}(\mathbf{q}) = \sum_n \frac{\Phi_{(0\tilde{I})(n\tilde{J})}^{\alpha\beta}}{M_{\tilde{I}} M_{\tilde{J}}} e^{i\mathbf{q}\cdot(\mathbf{R}_{(n\tilde{J})} - \mathbf{R}_{(0\tilde{I})})} \ . \tag{2.46}$$

Here, $\mathbf{D}(\mathbf{q})$ is the *dynamical matrix*, i.e., the Fourier transform of the mass-scaled force constants $\mathbf{\Phi}$ with respect to the distance of periodic replicas. In practice the sum can be truncated after a sufficient high value for n, so that we obtain a so called supercell containing n images of the unit cell. This supercell is now repeated periodically (see Fig. (2.2)). This means for example that the shortest vector connecting 2 atoms at opposite side of the supercell is typically directed to the last periodic image of the supercell. For a system with N atoms in the unit cell, we thus get $3N$ eigenvalues and -vectors at each reciprocal space point $\mathbf{q}$. Accordingly, the solution of the equations of motion is a superposition of harmonic oscillations

$$\mathbf{R}_I(t) = \mathbf{R}_I^{eq} + \text{Re}\left(\sum_{\mathbf{q},s} \frac{A_s(\mathbf{q})}{\sqrt{M_I}} \epsilon_{I,s}(\mathbf{q}) e^{i(\mathbf{q}\cdot\mathbf{R}_I - \omega_s(\mathbf{q})t)}\right) \tag{2.47}$$

with the amplitudes $A_s(\mathbf{q})$ and the wavevector $\mathbf{q}$. Please note that the amplitudes $A_s(\mathbf{q})$ and the respective occupation numbers $n_s(\mathbf{q}) = A_s^2(\mathbf{q})$ are **not** time-dependent and fully determined by the initial conditions, so that the individual oscillations are completely independent and decoupled. Accordingly, the motion is completely characterized by the eigenvectors and eigenfrequencies, i.e., the dispersion $\omega_s(\mathbf{q})$, which describes how the frequency of the phonon mode depends on its wavevector. Please note that also the derivative, i.e., the phonon group velocity

$$\mathbf{v}_s(\mathbf{q}) = \frac{\partial \omega_s(\mathbf{q})}{\partial \mathbf{q}} = \frac{1}{2\omega} \langle\epsilon_s(\mathbf{q})| \frac{\partial D(\mathbf{q})}{\partial \mathbf{q}} |\epsilon_s(\mathbf{q})\rangle \tag{2.48}$$

can be calculated directly from the dynamical matrix.

2 Theory

Given that Eq. (2.47) is the analytic solution for the nuclear dynamics in the harmonic potential, also the thermodynamic partition function of the system

$$Z = \prod_{\mathbf{q},s} \frac{e^{-\frac{\hbar\omega_s(\mathbf{q})}{k_B T}}}{1 - e^{-\frac{\hbar\omega_s(\mathbf{q})}{k_B T}}} \tag{2.49}$$

can be calculated. From this expression quantities such as the free energy [25]

$$F^{ha} = -k_B T \ln(Z) = \frac{1}{2} \sum_{\mathbf{q},s} \hbar\omega_s(\mathbf{q}) + k_B T \sum_{\mathbf{q}s} \ln(1 - e^{-\frac{\hbar\omega_s(\mathbf{q})}{k_B T}}) \tag{2.50}$$

and the specific heat C_V

$$C_V = \frac{1}{V} \left(\frac{\partial E^{ha}}{\partial T} \right)_V = \frac{1}{V} \sum_{\mathbf{q},s} \hbar\omega_s(\mathbf{q}) \frac{\partial n_s^{eq}(\mathbf{q})}{\partial T} = \frac{1}{V} \sum_{\mathbf{q},s} c_s(\mathbf{q}) \tag{2.51}$$

can be calculated with E^{ha} being the harmonic energy

$$E^{ha} = \sum_{\mathbf{q},s} \hbar\omega_s(\mathbf{q}) \left(\frac{1}{2} + n_s^{eq}(\mathbf{q}) \right). \tag{2.52}$$

It is important to note that phonons, since they are bosonic quasi particles, obey the Bose-Einstein distribution

$$n_s^{eq}(\mathbf{q}) = \frac{1}{e^{\frac{\hbar\omega_s(\mathbf{q})}{k_B T}} - 1} . \tag{2.53}$$

At low temperatures, this causes the typical T^3 behavior of the specific heat (see Fig. (3.7)). At elevated temperatures, C_V then approaches the classical, constant Dulong-Petit value $3Nk_b$ [35].

Most efficiently, equations such as (2.50) and (2.51) are numerically evaluated by introducing the phonon density of states

$$g(\omega) = \frac{1}{\Omega} \sum_s \int_{BZ} \delta(\omega - \omega_s(\mathbf{q})) d\mathbf{q} , \tag{2.54}$$

in which Ω denotes the volume of the Brillouin Zone. The thermodynamic expectation value Π for any operator $\pi(\omega_s(\mathbf{q}))$ that only implicitly depends on the wavevector $\mathbf{q}$ can then be immediately evaluated using

$$\Pi = \frac{1}{\Omega} \sum_s \int_{BZ} \pi_s(\mathbf{q}) d\mathbf{q} = \int \pi(\omega) g(\omega) d\omega . \tag{2.55}$$

Despite its usefullness, the harmonic approximation has severe limits. Due to the fact that the real PES is approximated close to the 0K equilibrium positions (see Fig.(2.2)), anharmonic effects become notable at higher temperatures, when large displacements from equilibrium occur. For instance, the temperature-dependence of phonon frequencies and their finite linewidth in spectra cannot be computed from the harmonic approximation

alone. Besides this quantitative anharmonic corrections, there are, however, physical phenomena that cannot even be understood qualitatively in a harmonic picture: Most importantly, the lattice expansion is zero and the vibrational thermal conductivity is infinite in this approximation. In the next two sections, we discuss these properties in more detail and explain how they can be assessed by accounting for anharmonic effects.

2.2.3 Anharmonic Effects: Lattice Expansion

In the static limit of immobile nuclei, the equilibrium volume V_0 and the respective lattice constants are defined via the minimum of the total energy of the system $V_0 = \min_V E_{tot}(V)$. At finite temperatures, however, the respective thermodynamic potential has to be minimized, e.g., the Helmholtz free energy $F(T, V)$ in the case of a canonical ensemble. Naturally, this introduces a temperature dependence in the equilibrium volume $V_0(T) = \min_V F(T, V)$. By neglecting the electronic contributions[4], the Helmholtz free energy can be expressed in the harmonic approximation as $F(T, V) \approx E_{tot}(V) + F^{ha}(T)$ using the definition of $F^{ha}(T)$ given in Eq. (2.50). However, $F^{ha}(T)$ does not depend on the volume, so that no lattice expansion (or contraction) occurs in this approximation. To assess and understand temperature dependent volumes and lattice constants, *anharmonic* effects have thus to be accounted for.

In the most intuitive approach, anharmonic effects are *effectively* introduced by explicitly accounting for the volume dependence of the force constants $\Phi_{IJ}^{\alpha\beta} \to \Phi_{IJ}^{\alpha\beta}(V)$. In this so called *quasi-harmonic* approximation [20], both the total energy $E_{tot}(V)$ and the phonon calculations $\Phi_{IJ}^{\alpha\beta}(V)$ are performed for a set of different volumes. The temperature dependent volume $V_0(T)$ and/or lattice constants are then determined by minimizing the resulting Helmholtz free energy

$$F(T, V) \approx E_{tot}(V) + F^{qha}(T, V) \quad \text{with} \quad F^{qha}(T, V) = F^{ha}(T, \Phi_{IJ}^{\alpha\beta}(V)), \qquad (2.56)$$

as shown in Fig. 2.3. The obtained equilibrium volumes $V_0(T)$ then allow to compute the volume expansion coefficient

$$\alpha(T) = \frac{1}{3V_0(T)} \left(\frac{\partial V_0(T)}{\partial T} \right)_V \qquad (2.57)$$

Beside some notable exceptions (see Ref. [20] and Sec. 3.2.3), $\alpha(T)$ is typically positive (lattice expansion): Larger volumes imply larger nearest neighbour distances and thus a smaller interaction (smaller force constants $\Phi_{IJ}^{\alpha\beta}$). In turn, this leads to lower eigenfrequencies $\omega_s(\mathbf{q})$ and thus to lower Helmholtz free energies due to entropic contributions.

---

[4]In solids with finite band gaps as the semiconductors of interest in this work, electronic contributions to the free energy are generally negligible [35].
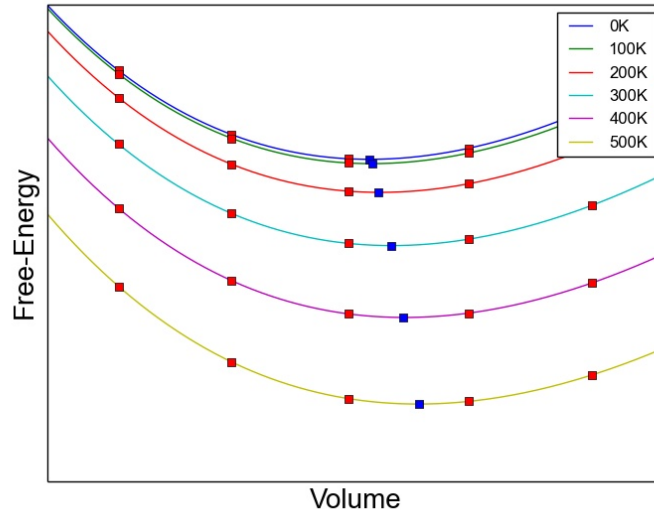
Figure 2.3: Birch-Murnaghan Equations in the quasi-harmonic approximation for Mg$_2$Si at different temperatures: The blue squares mark the volumes which minimize the free energy and the red points mark actual calculations.

An alternative approach to assess temperature dependent volumes and lattice constants starts from the definition of the volume expansion coefficient as thermodynamic derivative of the pressure at constant volume

$$\alpha(T) = \frac{1}{3B_0}\left(\frac{\partial P}{\partial T}\right)_{V_0(T)} = -\frac{1}{3B_0}\left(\frac{\partial^2 F(T,V)}{\partial T \partial V}\right)_{V_0(T)} , \qquad (2.58)$$

whereby B_0 is the bulk modulus. In praxis, this equation is approximated by taking the derivative at the equilibrium volume in the static limit $V_0(T) \to V_0$ (see Sec. 3.2.3 for a critical discussion of this approximation)

$$\alpha(T) \approx -\frac{1}{3B_0}\left(\frac{\partial^2 F(T,V)}{\partial T \partial V}\right)_{V_0} . \qquad (2.59)$$

This allows to use the Helmholtz free energy defined as $F(T,V_0) \approx E_{tot}(V_0) + F^{ha}(T)$, which yields [35]

$$\alpha = \frac{1}{3B_0}\sum_{\mathbf{q},s}\left(-\frac{\partial \hbar \omega_s(\mathbf{q})}{\partial V}\right)\frac{\partial n_s^{eq}(\mathbf{q})}{\partial T} = \frac{1}{3B_0}\sum_{\mathbf{q},s}\frac{\hbar \omega_s(\mathbf{q})\gamma_s(\mathbf{q})}{V}\frac{\partial n_s^{eq}(\mathbf{q})}{\partial T} = \frac{\gamma C_V}{3B_0} \qquad (2.60)$$

In the last steps, we have introduced the dimensionless, *mode-specific* Grüneisen parameter

$$\gamma_s(\mathbf{q}) = -\frac{V}{\omega_s(\mathbf{q})}\frac{\partial \omega_s(\mathbf{q})}{\partial V} , \qquad (2.61)$$

and the *overall* Grüneisen parameter

$$\gamma = \frac{\sum_{\mathbf{q},s} \gamma_s(\mathbf{q}) c_s(\mathbf{q})}{\sum_{\mathbf{q},s} c_s(\mathbf{q})} \tag{2.62}$$

using the definition of the mode-specific heat capacity $c_{\mathbf{q},s}$ given in Eq. (2.51). Two different approaches exist to evaluate the Grüneisen parameters:

Finite Differences: In the spirit of the quasi-harmonic approximation, these anharmonic effects can be *effectively* accounted for by explicitly investigating the volume dependence of the dynamical matrix. The Grüneisen parameters can then be determined via

$$\gamma_s(\mathbf{q}) = -\frac{1}{2\omega_s^2(\mathbf{q})} \frac{\partial \omega_s^2(\mathbf{q})}{\partial V} = -\frac{1}{2\omega_s^2(\mathbf{q})} \langle \epsilon_s(\mathbf{q})| \frac{\partial D(\mathbf{q})}{\partial V} |\epsilon_s(\mathbf{q})\rangle \;, \tag{2.63}$$

whereby the required derivative of the dynamical matrix is typically computed using a finite difference approach:

$$\frac{\partial D(\mathbf{q})}{\partial V} \approx \frac{D(\mathbf{q}, V_0 + \delta V) - D(\mathbf{q}, V_0 - \delta V)}{2\delta V} \;. \tag{2.64}$$

Explicit Anharmonicity: Alternatively, anharmonic effects can be incorporated by extending the Taylor expansion in Eq. (2.43) to an additional order:

$$E_{tot}^{anh} = E_{tot} + \frac{1}{2} \sum_{IJ,\alpha\beta} \Phi_{IJ}^{\alpha\beta} u_I^\alpha u_J^\beta + \frac{1}{6} \sum_{IJK,\alpha\beta\gamma} \Psi_{IJK}^{\alpha\beta\gamma} u_I^\alpha u_J^\beta u_K^\gamma \tag{2.65}$$

using the third order force constants

$$\Psi_{IJK}^{\alpha\beta\gamma} = \frac{\partial^3 E}{\partial R_I^\alpha \partial R_J^\beta \partial R_K^\gamma} \;. \tag{2.66}$$

These third order force constants are also not directly accessible within DFT: They can be either computed by application of first order perturbation theory [3] or again via finite differences:

$$\Psi_{IJK}^{\alpha\beta\gamma} = \frac{\partial^3 E}{\partial R_I^\alpha \partial R_J^\beta \partial R_K^\gamma} = \frac{\partial^2 \mathbf{F}}{\partial R_J^\beta \partial R_K^\gamma} = \frac{\partial \Phi_{IJ}}{\partial R_K^\gamma} \approx \frac{\Phi_{IJ}^{\alpha\beta}(\delta R_K^\gamma) - \Phi_{IJ}}{\delta R_K^\gamma} \tag{2.67}$$

The latter technique has been used in this work; the practical details are discussed in Sec. 3.2.4.

Please note that it is no longer possible to solve the equations of motion in the third order potential – neither analytically nor numerically via molecular dynamics [5]. To circumvent these problems, anharmonic effects stemming from the third order force constants are typically evaluated perturbatively by calculating expectation values stemming

---

[5]The asymmetry in the third order term makes such algorithms unstable.

from the potential Eq. (2.65) using the analytically know solutions of the harmonic approximation: For instance, the eigenfrequencies in harmonic approximation are given by

$$\omega_s^2(\mathbf{q}) = \sum_{IJ,\alpha\beta} \frac{\epsilon_{I,s}^{*\alpha}(\mathbf{q})\epsilon_{J,s}^{\beta}(\mathbf{q})}{\sqrt{M_I M_J}} \Phi_{IJ}^{\alpha\beta} e^{i\mathbf{q}\cdot(\mathbf{R}_J - \mathbf{R}_I)} \tag{2.68}$$

By replacing the harmonic force constants $\Phi_{IJ}^{\alpha\beta}$ with the respective perturbed expression including third order contributions $\hat{\Phi}_{IJ}^{\alpha\beta} = \Phi_{IJ}^{\alpha\beta} + \sum_{\gamma,K} \Psi_{IJK}^{\alpha\beta\gamma} u_K^\gamma$ one gets

$$\omega_s^2(\mathbf{q}) \quad \rightarrow \quad \sum_{IJ,\alpha\beta} \frac{\epsilon_I^{*\alpha}\epsilon_J^{\beta}}{\sqrt{M_I M_J}} \hat{\Phi}_{IJ}^{\alpha\beta} e^{i\mathbf{q}\cdot(\mathbf{r}_J - \mathbf{r}_I)} \tag{2.69}$$

$$= \quad \omega_s^2(\mathbf{q}) + \sum_{IJ,\alpha\beta} \frac{\epsilon_{I,s}^{*\alpha}(\mathbf{q})\epsilon_{J,s}^{\beta}(\mathbf{q})}{\sqrt{M_I M_J}} \left(\sum_{\gamma,K} \Psi_{IJK}^{\alpha\beta\gamma} u_K^\gamma \right) e^{i\mathbf{q}\cdot(\mathbf{R}_J - \mathbf{R}_I)} . \tag{2.70}$$

This expression and also its derivatives can be evaluated numerically.

Exemplarily, we discuss this approach for the Grüneisen tensors, i.e., the dimensionless derivative of the eigenfrequencies

$$\gamma_s^{\mu\nu}(\mathbf{q}) = -\frac{1}{\omega_s(\mathbf{q})} \frac{\partial \omega_s(\mathbf{q})}{\partial \epsilon_{\mu\nu}} = -\frac{1}{2\omega_s^2(\mathbf{q})} \frac{\partial \omega_s^2(\mathbf{q})}{\partial \epsilon_{\mu\nu}} \tag{2.71}$$

with respect to a strain $\epsilon_{\mu\nu}$ that acts on real space coordinates as

$$R_\alpha(\epsilon) = \sum_\beta (\delta_{\alpha\beta} + \epsilon_{\alpha\beta}) R_\beta(0) . \tag{2.72}$$

The strain derivative can then be written as [32]:

$$\frac{\partial \hat{\Phi}_{IJ}^{\alpha\beta}}{\partial \epsilon_{\mu\nu}} = \sum_{\gamma,K} \Psi_{IJK}^{\alpha\beta\gamma} \delta_{\mu\gamma} R_K^\nu . \tag{2.73}$$

Using the formalism introduced above, one gets the Grüneisen tensors to first order:

$$\gamma_s^{\mu\nu}(\mathbf{q}) = -\frac{1}{2\omega_s^2(q)} \sum_{IJK,\alpha\beta\gamma} \frac{\epsilon_{I,s}^{*\alpha}(\mathbf{q})\epsilon_{J,s}^{\beta}(\mathbf{q})}{\sqrt{M_I M_J}} \Psi_{IJK}^{\alpha\beta\gamma} \delta_{\mu\gamma} R_K^\nu e^{i\mathbf{q}\cdot(\mathbf{R}_J - \mathbf{R}_I)} . \tag{2.74}$$

Please note that this Grüneisen tensors are a generalization of the Grüneisen parameters

$$\gamma_s(\mathbf{q}) = \frac{\text{tr}(\gamma_s^{\mu\nu}(\mathbf{q}))}{3} \tag{2.75}$$

introduced in Eq. (2.61), whereby "tr" denotes the trace.

2.2.4 Anharmonic Effects: Lattice Thermal Conductivity

The thermal conductivity tensor $\kappa_{\alpha\beta}$, which describes the capability of a material to conduct heat, is another prominent example of a physical quantity that can only be understood if anharmonic effects are taken into account. Formally, the thermal cconductivity is defined through Fourier's law

$$J_\alpha = -\kappa_{\alpha\beta}\nabla_\beta T \ , \tag{2.76}$$

in which it serves as proportionality constant between the cartesian components of the applied temperature gradient ∇T and the heat flux $\mathbf{J}$, which naturally develops to contrast ∇T and to re-establish equilibrium. Generally, the thermal conductivity consists of three different contributions

$$\kappa = \kappa_{\text{phonon}} + \kappa_{\text{electron}} + \kappa_{\text{photon}} \ . \tag{2.77}$$

In this work, we limit ourselves to dicuss the *lattice* or *phonon* thermal conductivity κ_{phonon}, since it is the dominant [35] contribution for the system of interests in this work (semiconductors and insulators at non-incandescent temperatures).

The fact that such heat transport effecrs cannot be assessed in a purely harmonic approximation already becomes obvious from the respective microscopic expression for the heat flux formulated in the phonon picture [36]

$$\mathbf{J} = (2\pi)^3 \sum_s \int \hbar\omega_s(\mathbf{q})n_s(\mathbf{q},t)\mathbf{v}_s(\mathbf{q})d\mathbf{q} \approx \frac{1}{V_0}\sum_{\mathbf{q},s} \hbar\omega_s(\mathbf{q})n_s(\mathbf{q},t)\mathbf{v}_s(\mathbf{q}) \ . \tag{2.78}$$

Here V_0 denotes the volume of the unit cell. In this expression, each of the modes with occupation number $n_s(\mathbf{q})$ contribute to the heat flux, since they travel with the group velocity $\mathbf{v}_s(\mathbf{q})$ and carry the energy $\hbar\omega_s(\mathbf{q})$. In the harmonic approximation, however, all quantities that enter Eq. (2.78) stay constant over time: Even the occupation numbers $n_s(\mathbf{q},t) = n_s^{eq}(\mathbf{q})$ are fully determined by the initial conditions (see Sec. 2.2.2), since all modes are decoupled. Accordingly, the heat flux $\mathbf{J}$ in equilibrium is exactly zero in the harmonic approximation at all times, since the contributions with opposite wavevectors cancel out due to the fact that

$$\omega_s(\mathbf{q}) = \omega_s(-\mathbf{q}) \quad \text{and} \quad n_s(\mathbf{q},t) = n_s(-\mathbf{q},t) \quad \text{but} \quad \mathbf{v}_s(\mathbf{q}) = -\mathbf{v}_s(-\mathbf{q}) \ . \tag{2.79}$$

Therefore, Eq. (2.76) is not fulfilled in the harmonic approximation.

To assess thermal conductivities, it is thus necessary to take anharmonic effects explicitly into account. This can be achieved by explicitly investigationg the dynamics on the anharmonic potential energy surface in molecular dynamics approaches [29] or perturbatively [26]. In this work, only the latter approach is used; for the sake of conciseness, we will thus limit the discussion in this thesis to this technique. Also, we restrict the derivation to the cubic isotropic case which allows us to write $\kappa = \kappa_{xx} = \kappa_{yy} = \kappa_{zz}$. A

more general and detailed derivation can for instance be found in Ref. [36] and references therein.

To account for anharmonic effects, we first introduce the non-equilibrium occupation numbers $n_s(\mathbf{q})$ by introducing a mode specific deviation $\xi_s(\mathbf{q})$:

$$
\begin{aligned}
n_s(\mathbf{q}) &= \frac{1}{e^{\frac{\hbar\omega_s(\mathbf{q})}{k_B T} - \xi_s(\mathbf{q})} - 1} \\
&\approx n_s^{eq}(\mathbf{q}) + \left(\frac{\partial n_s(\mathbf{q})}{\partial \xi_s(\mathbf{q})}\right)_{\xi_s(\mathbf{q})=0} \xi_s(\mathbf{q}) = n_s^{eq}(\mathbf{q}) + [n_s^{eq}(\mathbf{q})(n_s^{eq}(\mathbf{q})+1)]\,\xi_s(\mathbf{q}) \\
&= n_s^{eq}(\mathbf{q}) + \frac{k_B T^2}{\hbar\omega_s(\mathbf{q})}\frac{\partial n_s^{eq}(\mathbf{q})}{\partial T}\xi_s(\mathbf{q})\;.
\end{aligned}
\tag{2.80}
$$

When performing the Taylor expansion around equilibrium in the second step, we inherently assume that the deviations from equilibrium are small compared to the actual occupation numbers in equilibrium. Accordingly, the non-equilibrium occupation numbers $n_s(\mathbf{q})$ must fulfill the linearized Boltzmann equation

$$
\mathbf{v}_s(\mathbf{q}) \cdot \nabla T \frac{\partial n_s^{eq}(\mathbf{q})}{\partial T} = \left(\frac{\partial n_s(\mathbf{q})}{\partial t}\right)_{scatt}
\tag{2.81}
$$

in the steady state. Here, the left hand side (drift term) describes the evolution of the non-equilibrium population due to a temperature gradient in the absence of phonon-phonon interaction. Conversely, the right hand side counterbalance this drift due to scattering processes. To describe them, the *single mode relaxation time approximation* is commonly employed: This implies that explicit correlations between the non-equilibrium occupation numbers of the different modes can be neglected, so that the scattering of one specific mode $(s', \mathbf{q}')$ can be determined by assuming all other modes to follow the respective equilibrium distribution: $n_s(\mathbf{q}) = n_s^{eq}(\mathbf{q})$ for all $(s, \mathbf{q}) \neq (s', \mathbf{q}')$. In this approach, the right hand side of Eq. (2.81) can be approximated as

$$
\left(\frac{\partial n_s(\mathbf{q})}{\partial t}\right)_{scatt} \approx -\frac{\xi_s(\mathbf{q})}{\tau_s(\mathbf{q})}\frac{k_B T^2}{\hbar\omega_s(\mathbf{q})}\frac{\partial n_s^{eq}(\mathbf{q})}{\partial T}
\tag{2.82}
$$

whereby the mode specific relaxation times $\tau_s(\mathbf{q})$ have been introduced. Combining Eq. (2.81) and Eq. (2.82) yields an expression for $\xi_s(\mathbf{q})$ and thus for the $n_s(\mathbf{q})$ defined in Eq. (2.80) that can be inserted into Eq. (2.78):

$$
\mathbf{J} = -\frac{1}{V_0 k_B T^2}\sum_{s\mathbf{q}}\hbar\omega_s(\mathbf{q})\frac{\partial n_s^{eq}(\mathbf{q})}{\partial T}\tau_s(\mathbf{q})\mathbf{v}_s(\mathbf{q})(\mathbf{v}_s(\mathbf{q}) \cdot \nabla T)\;.
\tag{2.83}
$$

For the isotropic case, a comparison with Fourier's law (2.78) yields:

$$
\kappa = \frac{1}{3V_0}\sum_{q,s}\mathbf{v}_s(\mathbf{q})^2 c_s(\mathbf{q})\tau_s(\mathbf{q})\;.
\tag{2.84}
$$

Most of the quantities $(\mathbf{v}_s(\mathbf{q}), c_s(\mathbf{q}))$ entering κ as defined in Eq. (2.84) can be readily

computed in the harmonic approximation. The lifetime $\tau_s(\mathbf{q})$, however, is infinite in this approximation, due the absence of scattering $n_s(\mathbf{q}) = n_s^{eq}(\mathbf{q})$ discussed before. Formally, the thermal conductivity is thus also infinite in this approximation.

If anharmonic effects are taken into account, the lifetimes can be determined via

$$\tau_s(\mathbf{q}) = \frac{1}{2\Gamma_s(\mathbf{q})} \tag{2.85}$$

from the imaginary part of the self energy $\Gamma_s(\mathbf{q})$. If only the third order force constants $\Psi_{IJK}^{\alpha\beta\gamma}$ (introduced in Sec. 2.2.3 before) are taken into account, this self energy is given by:

$$\Gamma_s(\mathbf{q}) = \frac{18\pi}{\hbar^2} \sum_{\mathbf{q}'s',\mathbf{q}''s''} |\Psi_{s,s',s''}(\mathbf{q},\mathbf{q}',\mathbf{q}'')|^2 [(n_{s'}^{eq}(\mathbf{q}') + n_{s''}^{eq}(\mathbf{q}'') + 1)\delta(\omega - \omega_{s'}(\mathbf{q}') - \omega_{s''}(\mathbf{q}''))$$
$$+ (n_{s'}^{eq}(\mathbf{q}') - n_{s''}^{eq}(\mathbf{q}''))(\delta(\omega + \omega_{s'}(\mathbf{q}') - \omega_{s''}(\mathbf{q}'')) - \delta(\omega - \omega_{s''}(\mathbf{q}') + \omega_{s''}(\mathbf{q}''))] \tag{2.86}$$

The $\Psi(\mathbf{q}s,\mathbf{q}'s',\mathbf{q}''s'')$ are the Fourier transformed third order force constants $\Psi_{IJK}^{\alpha\beta\gamma}$:

$$\Psi_{s,s',s''}(\mathbf{q},\mathbf{q}',\mathbf{q}'') = \frac{1}{3!\sqrt{N_0}} \sum_{IJK,\alpha\beta\gamma} \epsilon_{I,s}^{\alpha}(\mathbf{q})\epsilon_{J,s'}^{\beta}(\mathbf{q}')\epsilon_{K,s''}^{\gamma}(\mathbf{q}'')$$
$$\times \sqrt{\frac{\hbar}{2M_I\omega_s(\mathbf{q})}}\sqrt{\frac{\hbar}{2M_J\omega_{s'}(\mathbf{q}')}}\sqrt{\frac{\hbar}{2M_K\omega_{s''}(\mathbf{q}'',s'')}}$$
$$\times \Psi_{IJK}^{\alpha\beta\gamma} e^{i\mathbf{q}\cdot\mathbf{R}_I} e^{i\mathbf{q}'\cdot\mathbf{R}_J} e^{i\mathbf{q}''\cdot\mathbf{R}_K} \Delta(\mathbf{q}+\mathbf{q}'+\mathbf{q}'') \tag{2.87}$$

Here, the factor $\Delta(\mathbf{q}+\mathbf{q}'+\mathbf{q}'')$ ensures momentum conservation and is thus 1 if $\mathbf{q}+\mathbf{q}'+\mathbf{q}''$ corresponds to a reciprocal lattice vector and 0 otherwise. Please note that the expressions (2.85)-(2.87) can be derived directly in a quite lengthy process from the third order Hamiltonian, as detailed in Ref. [38] for instance.

The described approach has so far been used successfully in a series of studies [27, 26]. However, it also suffers from some limitations:

- It has been shown that the *single relaxation time approximation* can fail [28], e.g., in systems with very long lifetimes, e.g., graphene [23]. In this case, the linearized Bolzmann transport equation (2.81) needs to be solved numerically or directly [37]

- So far, efforts to systematically and accurately assess the anharmonicity beyond the third order force constants from first principles have remained elusive: On the one hand, perturbational approaches based on density-functional perturbation theory [21] would require the second order response in the density [22] for computing higher-order force constants. On the other hand, finite difference approaches would become excruciatingly expensive due to the combinatorial explosion of elements included in higher-order force constants. Accordingly, very anharmonic systems cannot be

treated in this approach but require *ab initio* molecular dynamics simulations that systematically probe the complete anharmonic phase space. The thermal conductivity can the be determined from the Green-Kubo relations [29, 30]. Please note that higher-order force constants can be extracted from such *ab initio* molecular dynamics trajectories as well [19]. For this purpose, *machine-learning* techniques have been recently proven to be useful [31].

Eventually, it is important to note that even in the best case the computational cost of first-principles calculations in the single relaxation time approximation is quite involved, in particular for systems with low symmetry and/or many atoms in the unit cell. Most importantly, this is the case whenever defects, impurities, or disorder are present and need to modeled in a supercell approach (see Sec. 3.2.1). For such systems, this has so far prevented systematic first-principles, *high-throughput* studies across the periodic table. In various studies, this has been circumvented by developing and using various semi-empirical approximations to estimate the lifetime. Some representative approaches are shortly summarized below; their validity and usability is discussed in more detail in Sec. 3.3.

Constant Relaxation Time Approximation: In this most simple approximation, the lifetime is assumed to be a constant that is independent from $\mathbf{q}$ and s, so that one gets

$$\kappa = \frac{1}{3V_0} \sum_{q,s} \mathbf{v}_s(\mathbf{q})^2 c_s(\mathbf{q}) \tau_s(\mathbf{q}) \to \frac{\tau}{3V_0} \sum_{q,s} \mathbf{v}_s(\mathbf{q})^2 c_s(\mathbf{q}) \tag{2.88}$$

The sum and integral can be fully evaluated within reasonable computational cost in the harmonic approximation. The lifetime τ is then typically estimated or fitted to known experimental or theoretical results (see Sec. 3.3).

Slack's Method: Following the reasoning of the constant relaxation time approximation, Slack [39] proposed an analytic expression for the phonon lifetimes

$$\frac{1}{\tau_s(\mathbf{q})} = p\omega_s^2(\mathbf{q})\frac{T}{\Theta_D}e^{-\frac{\Theta}{T}} \tag{2.89}$$

for temperatures close to Debye temperature Θ_D. in Slack's original work [39], p is an empirical parameter that needs to be estimated. Madsen et al. [40] improved this approach by determing p from different other models, e.g., by using Grüneisen paramters.

Constant Mean Free Path Approximation: Formally, this approximation is conceptually very similar to the constant relaxation time approximation. In this case, however, the mean free path

$$\Lambda_s(\mathbf{q}) = \tau_s(\mathbf{q})|\mathbf{v}_s(\mathbf{q})| \overset{!}{=} \Lambda \tag{2.90}$$

is assumed to be a constant parameter Λ. In turn, this yields the following expression for the thermal conductivity

$$\kappa = \frac{\Lambda}{3V_0} \sum_{q,s} \mathbf{v}_s(\mathbf{q}) c_s(\mathbf{q}). \tag{2.91}$$

For instance, Galli et al. [41] have used this approach in a reduced form

$$\kappa = \frac{1}{3V_0} C_V v \Lambda \tag{2.92}$$

by assuming that a single effective group velocity v (Debye model) can be used to model thermal conductivities.

3 Properties of Pristine Magnesium Silicide

Mg_2Si is a semiconducting material that crystallizes in an antifluorite structure (Space group $225/Fm\bar{3}m$). In recent years, it has been regarded as a promising material for thermoelectric applications due to its relatively cheap price, high melting temperature (~ 1400 K), and its non-toxic composition. In its pristine form, its figure of merit ZT has been measured to be between 0.2 and 1.1 [45] depending on the manufacturing process. As discussed in Sec. 1, doping is regarded as a promising route to increase ZT and thus the thermoelectric efficiency even further.

Although Mg_2Si is certainly not the most promising candidate for a high-efficiency thermoelectric, it is the ideal test case for first-principles calculations in this field. On the one hand, it has only three atoms in the unit cell, which makes it preferable to other, more complex thermoelectric materials such as clathrates (46 atom in a unit cell at least) for computational reasons. On the other hand, it does not contain any heavy elements, which allows to neglect computationally tricky effects such as the spin-orbit coupling, which makes it preferable to classic thermoelectric materials such as Bi_2Te_3 and Pb_2Te_3.

3.1 Basic Properties of Magnesium Silicide

In a first step, we investigated the geometric and lattice properties of Mg_2Si, i.e., the lattice constant a_0, the bulk modulus B_0, and its derivative B_0' in the *anti-fluorite* structure (fcc). For this purpose, five individual DFT calculations were performed for lattice constants $a_0^{(i=1\cdots 5)}$ in the range $\pm 3\%$ around the experimental lattice constant 6.34 Å [42]. The resulting total energies $E_{tot}(a_0^i)$ were fitted with the Birch-Murnaghan equation of state [50, 51] to determine a_0, B_0, and B_0'. As detailed in the appendix 7, these calculations were performed for different numerical settings to investigate the convergence of these properties of interest with respect to these parameters. This revealed that using an electronic $(12 \times 12 \times 12)$ **k**-grid, FHI-aims' *"tight"* integration grids, and a Si tier 1 and Mg tier 2 basis set yields not only qualitatively correct, but even quantitatively sound results, e.g., lattice constants a_0 are converged up to ± 0.01 Å. Accordingly, these exact settings were used also for all other calculations presented in this thesis.

Furthermore, the dependence of a_0, B_0, and B_0' on the chosen XC-functional was investigated by performing calculations in the local (LDA) and semi-local (GGA: PBE, PBEsol)

Functional	a_0 (Å)	B_0 (eV/Å)	B_0'
LDA	6.27	0.36	4.10
PBE	6.37	0.34	3.87
PBEsol	6.33	0.35	3.91
PBE0	6.33	0.36	3.83
Exp.	$6.34^{a,b}$	0.37^b	–
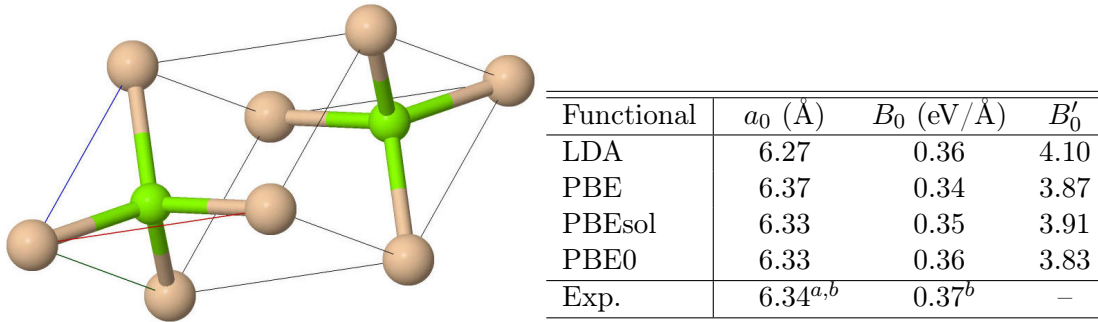
Figure 3.1 & Table 3.1: Left: Primitive unit cell of pristine Mg_2Si (Mg brown, Si green). Right: Lattice constant a_0, bulk modulus B_0, and its derivative B_0' of Mg_2Si as determined by a Birch-Murnaghan fit to DFT data computed for different XC functionals.
[a] Ref. [42] [b] Ref. [43]

E_{gap} (eV)	this work				from literature	
	LDA	PBE	PBEsol	PBE0	Exp. [46]	LDA [47]
$\Gamma \leftrightarrow \Gamma$	1.98	1.82	1.87	3.14	2.2	1.55
$\Gamma \leftrightarrow X$	0.14	0.23	0.13	1.16	-	

Table 3.2: Values for the direct ($\Gamma \leftrightarrow \Gamma$) and indirect ($\Gamma \leftrightarrow X$) Electronic bandgap of Mg_2Si calculated with LDA, PBE, PBEsol, and PBE0.

approximation and comparing the outcome to more involved calculations using a hybrid functional (PBE0). As shown in Tab. 3.1, LDA exhibits its typical "overbinding" (too small lattice constants, large B_0 and B_0'), whereas PBE "underbinds" and thus exhibits the opposite trend. PBEsol lies in between LDA and PBE; it also yields the closest result with respect to the PBE0 calculation and experiment [42]. Generally, however, these geometric properties are not particularly sensitive on the chosen XC-functional.

In Fig. (3.2) the electronic band structure for LDA, PBE, PBEsol, and PBE0 is shown. While all band structures look qualitatively similar it is obvious that the band gap for LDA, PBE, and PBEsol is much smaller than the band gap with PBE0 (see Tab. 3.2). A more detailed investigation of the electronic structure in terms of a *partial* density of states (PDOS) [1] reveals that both the valence band and the conduction band are highly hybridized indicating a partially covalent character of the bonding instead of purely ionic character (see Fig. 3.3).

---

[1]In *partial* density of states the contribution of the individual atoms to the full density of states is disentangled by preforming a Mulliken population analysis, i.e., by projecting it onto individual atomic orbitals.
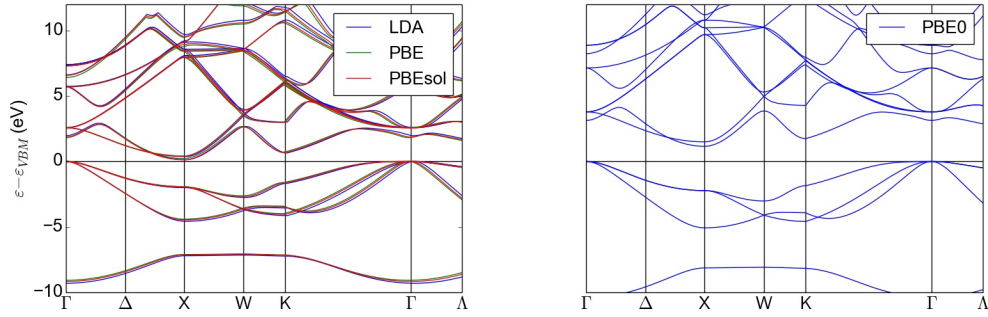
Figure 3.2: Electronic band structure of Mg_2Si close to the Fermi level as computed with DFT between high-symmetry points [33] at the respective equilibrium geometries (see Tab. 3.1) for the LDA, PBE, PBEsol (all left), and for the PBE0 XC-functional (right). The different band structures were aligned in such a way that the valence band maximum (VBM) corresponds to the absolute zero.
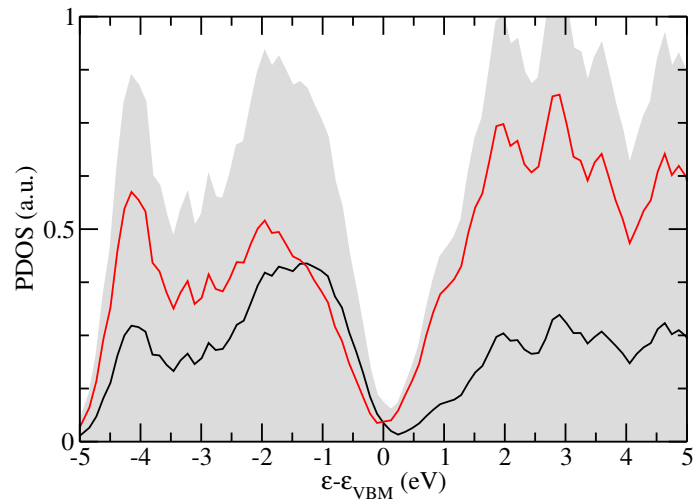
Figure 3.3: Partial density of states of Mg_2Si calculated using PBEsol.
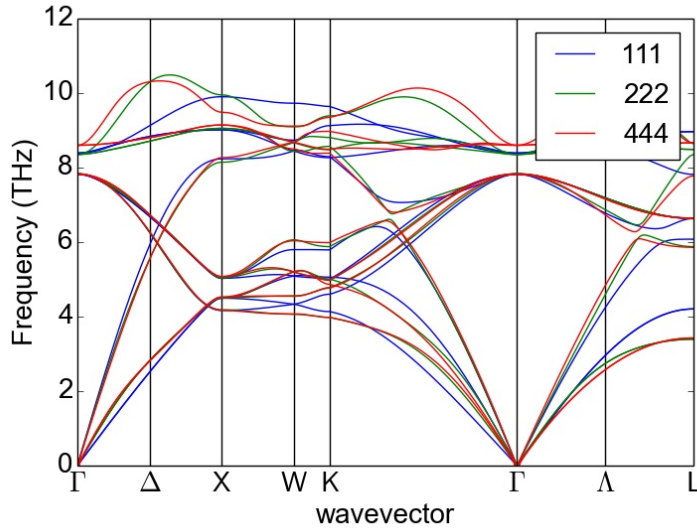
Figure 3.4: Phonon Bandstructure of Mg$_2$Si in the first (111), second (222), and fourth (444) cubic supercell calculated with PBEsol and light integration grids

3.2 Vibrational Properties of Magnesium Silicide

3.2.1 Methodology

As discussed in detail in Sec. 2.2.2, an assessment of the vibrational properties in the harmonic and/or quasi-harmonic approximation requires to compute the force constants $\Phi_{IJ}^{\alpha\beta}$, i.e., the Hessian of the potential energy surface. In this work, a finite difference approach as proposed by Parlinski, Li, and Kawazoe [24] and implemented in the *phonopy* package [25] was used for this purpose. This requires to compute the forces $\mathbf{F}_I(\Delta\mathbf{R}_J)$ acting on the individual atoms I under a small displacement $\Delta\mathbf{R}_J$ of atom J from equilibrium. In a second step, the Hessian is computed using the forward difference

$$\Phi_{IJ}^{\alpha\beta} = \frac{\partial E}{\partial R_I^\alpha \partial R_J^\beta} = \frac{\partial F_I^\alpha}{\partial R_J^\beta} \approx \frac{F_I^\alpha(\delta R_J^\beta)}{\delta R_J^\beta} \ . \tag{3.1}$$

In a naive approach, determining the $3N \times 3N$ force constants for a system with N atoms in the unit cell would thus require the forces for $3N$ individual displaced geometries. In *phonopy* [25], this amount is significantly reduced by exploiting symmetry, e.g., only 2 (and not 288) force evaluations are required in the case of Mg$_2$Si in a 96-atom supercell.

It this context it is important to stress that it is necessary to perform these force evaluations in supercells to assess the Hessian in the extended system for displacements $n\tilde{I}$: As discussed in Sec. 2.2.2, $\tilde{I}$ is the index for the atoms in the unit cell and n denotes the specific periodic image of this atom. The extended Hessian $\Phi_{(0\tilde{I})(n\tilde{J})}^{\alpha\beta}$ can then be used to determine the

wavevector $\mathbf{q}$ dependence of the frequencies via the dynamical matrix (also see Sec. 2.2.2):

$$D_{\tilde{I}\tilde{J}}^{\alpha\beta}(\mathbf{q}) = \sum_n \frac{\Phi_{(0\tilde{I})(n\tilde{J})}^{\alpha\beta}}{M_{\tilde{I}}M_{\tilde{J}}} e^{i\mathbf{q}\cdot(\mathbf{R}_{(n\tilde{J})}-\mathbf{R}_{(0\tilde{I})})} \ . \tag{3.2}$$

Formally, only a finite number of frequencies $\omega_s(\mathbf{q_i})$ with wavevectors $\mathbf{q}_i$ that are commensurate with the supercell can be assessed exactly in a finite supercell. Given that the forces and the force constants decay with the distance, the Fourier transformation in Eq. (3.2) can be truncated and the full spectrum $\omega_s(\mathbf{q})$ can be obtained nonetheless by Fourier interpolation [24]. Still, the convergence of the quantities of interest with respect to the chosen supercell size has to be carefully inspected in practice. For Mg$_2$Si, this has been done by performing calculations in the conventional cubic $(1 \times 1 \times 1)$, $(2 \times 2 \times 2)$, and $(4 \times 4 \times 4)$ supercell containing 12 (4), 96 (32), and 768 (256) atoms (Mg$_2$Si unit cells), respectively. The respective phonon band structures are shown in Fig. 3.4: In comparison with the fully supercell converged $(4 \times 4 \times 4)$ band structure, the $(1 \times 1 \times 1)$ band structure exhibits both qualitative and quantitative differences, e.g. over- and underestimated dispersion in the low frequency spectrum, and large deviations at the high-symmetry points Λ and L. Conversely, the $(2 \times 2 \times 2)$ band structure is essentially indistinguishable from the $(4 \times 4 \times 4)$ band structure at low frequencies (< 8 THz); for the high-frequency region, all qualitative features are well reproduced and only small quantitative deviances with a maximal value < 0.5 THz (≈ 2 meV) are observed. Therefore, all calculations presented in this and the next section were performed in a $(2 \times 2 \times 2)$ supercell, since this obviously is a good compromise between computational cost and accuracy.

Please note that the exact same conceptual approach was also used to determine the third order force constants $\Psi_{IJK}^{\alpha\beta\gamma}$ via

$$\Psi_{IJK}^{\alpha\beta\gamma} = \frac{\partial^3 E}{\partial R_I^\alpha \partial R_J^\beta \partial R_K^\gamma} = \frac{\partial^2 F_I^\alpha}{\partial R_J^\beta \partial R_K^\gamma} = \frac{\partial \Phi_{IJ}^{\alpha\beta}}{\partial R_K^\gamma} \approx \frac{\Phi_{IJ}^{\alpha\beta}(\delta R_K^\gamma) - \Phi_{IJ}^{\alpha\beta}}{\delta R_K^\gamma} \ . \tag{3.3}$$

Obviously, these calculations are always at least one order of magnitude more expensive than the corresponding Hessian calculations, given that $3N \times 3N \times 3N$ elements need to be determined. In this work, the *phono3py* package [26] was used to perform these calculations. Again, this package makes extensive use of symmetry to reduce the computational effort. For instance, "only" 258 (and not more than 80000) force evaluations are required for Mg$_2$Si in a 96-atom supercell.

In this context, it is important to note that for the practical harmonic (Hessian) calculations the *phonopy-FHI-aims* [2] interface between *phonopy* and *FHI-aims* was employed. However, no interface between *phono3py* and *FHI-aims* existed at the beginning of this thesis. Developing such an interface that can read, write, and convert both the input and output formats of *phono3py* and *FHI-aims* was an integral part of this thesis' work that enabled

---

[2]The *phonopy-FHI-aims* interface was originally developed by Jörg Meyer *et al.* during his time at the Theory Department of the Fritz-Haber-Institute of the Max-Planck-Society.
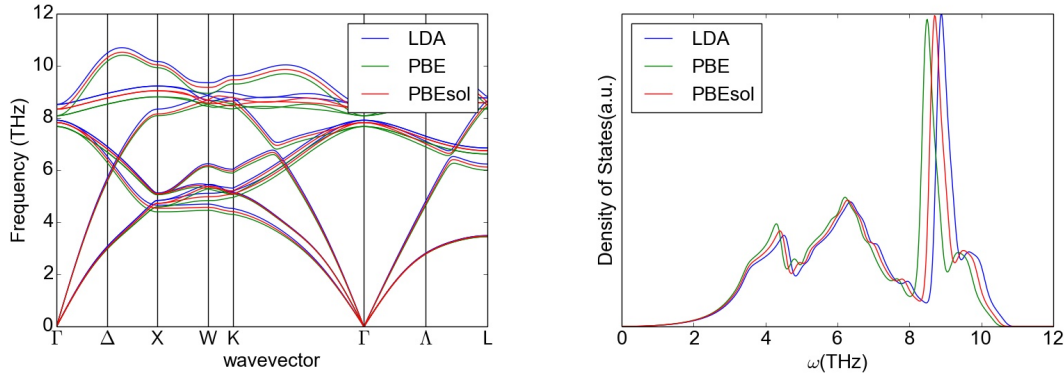
Figure 3.5: Phonon band structure $\omega_s(\mathbf{q})$ (left) and phonon density of states $g(\omega)$ (right) of Mg_2Si computed at the respective equilibrium volumes (see Tab. I) for the LDA, PBE, and PBEsol XC-functionals. The density of states $g(\omega)$ was computed using an extended $(60 \times 60 \times 60)$ $\mathbf{q}$-grid and a Gaussian smearing of 0.1 THz.

the calculations discussed below.

3.2.2 Vibrational Properties of Mg_2Si in the Harmonic Approximation

The plots in Fig. (3.5) show the converged phonon band structure $\omega_s(\mathbf{q})$ and density of states $g(\omega)$ of Mg_2Si at the equilibrium volume in the static limit (lattice constant a_0 given in Tab. I). To qualitatively classify the vibrational properties of Mg_2Si, we compare its phonon band structure to the ones of Si and CuCl (see Fig. 3.6), two materials known for their strong harmonicity/anharmonicity. For Mg_2Si, the highest observed (optical) frequencies are in the order of magnitude of 11 THz and thus lower than the ones in Si (15 THz) and slightly larger than CuCl (7.5 THz). Qualitatively, the phonon band structure of Mg_2Si looks more similar to the one of Si than the one of CuCl: For both Mg_2Si and Si, highly dispersive modes are observed across the whole range. In contrast to CuCl, no gap is observed between the acoustic and optical modes.

With respect to the chosen XC functional, the same trends discussed for the lattice constants in Sec. 3.1 are observed (see Fig. 3.5). LDA tends to "overbind" so that also the frequencies are generally higher (stiff bonding), whereas PBE tends to underbind and thus yields generally lower frequencies. As in the case of the lattice constant, PBEsol places itself between PBE and LDA. Most prominently, this trend is observed for the high frequency optical phonons between 8 and 10 THz in the also shown density of states. Again, however, the vibrational properties of Mg_2Si are not particularly sensitive on the chosen XC functional.

Additionally, Fig. 3.7 shows the thermodynamic potentials (internal energy U, entropy S, and free energy $F = U - TS$) and the respective specific heat c_V of Mg_2Si, which were computed from the harmonic force constants using the techniques detailed and discussed
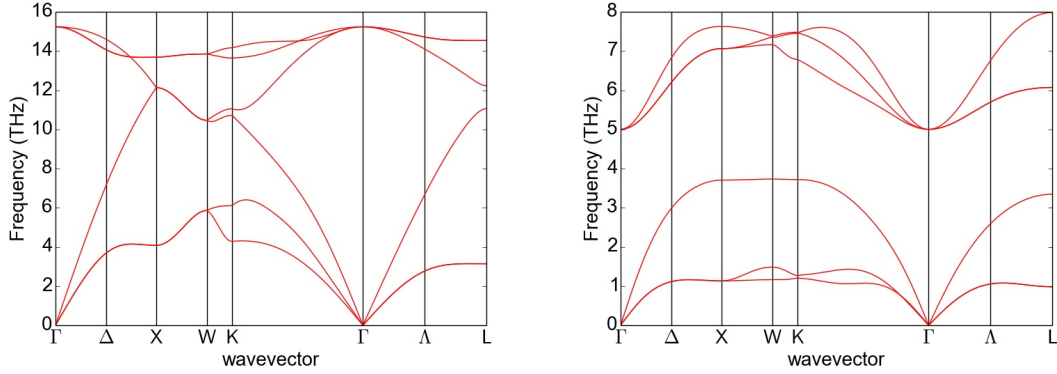
Figure 3.6: Phonon band structure $\omega_s(\mathbf{q})$ of Si in the diamond structure (left) and CuCl (right) computed using the PBEsol functional. The computational settings used for these two systems are summarized in Appendix 7.
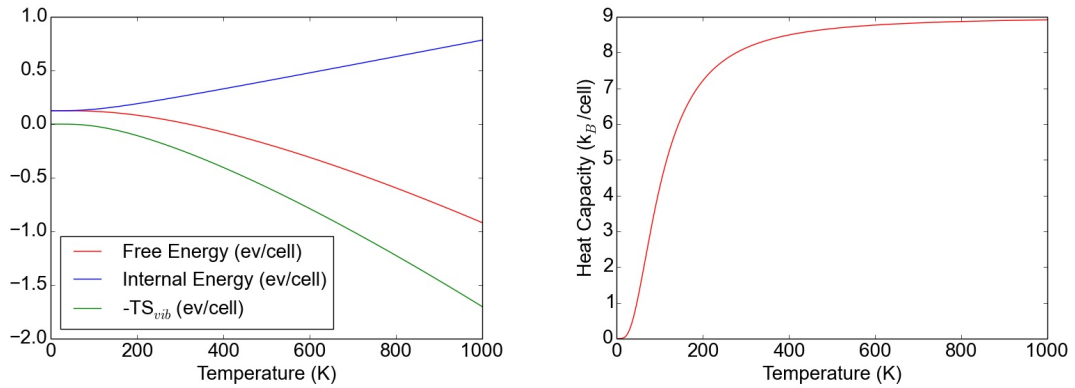
Figure 3.7: Thermodynamic potentials (internal energy U, entropy S, and free energy $F = U - TS$) of Mg_2Si (left) and the respective specific heat c_V (right) computed in the harmonic approximation (DFT-PBEsol). An extended $(60 \times 60 \times 60)$ $\mathbf{q}$-point grid was used to determine U, S, F, and c_V.
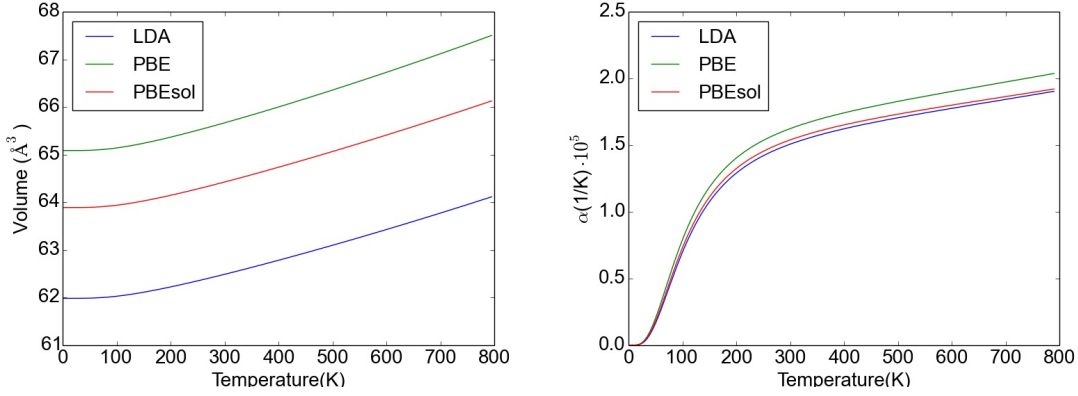
Figure 3.8: Temperature dependent equilibrium volume $V_0(T)$ (left) and thermal expansion coefficient $\alpha(T)$ (right) of Mg_2Si computed using the quasi-harmonic approximation and the LDA, PBE, and PBEsol XC-functionals.

in Sec. 2.2.2. Due to the use of the Bose-Einstein distribution (2.53) for the occupation number of the phonons, quantum-mechanical effects in the nuclear dynamics are inherently accounted for. Accordingly, we observe the typical quantum-mechanical T^3 dependence of the specific heat c_V at low temperatures. The classical Dulong-Petit limit (constant c_V) is only reached at temperatures above 400 K. This is consistent with the calculated and measured values for the Debye temperature (434 K as detailed in Sec. 3.3 and 417 K measured at 300K [42], respectively).

3.2.3 Vibrational Properties of Mg_2Si in the Quasi-Harmonic Approximation

As a first step in the investigation of anharmonic effects, the temperature dependent volume $V_0(T)$ of Mg_2Si was computed using the *quasi harmonic approximation* discussed in Sec. 2.2.2. Along the lines of the Birch-Murnaghan fits discussed in Sec. 3.1 to determine the equilibrium volume in the static limit, both total energy and phonon calculations were performed for five different volumes $V_0^{i=1..5}$. The respective free energies $F(V_i^0, T)$ were computed using Eq. (2.56) for temperatures between 0 and 800 K and then fitted using the Birch-Murnaghan equation of state to determine the temperature dependent volume $V_0(T)$. The thermal expansion $\alpha(T)$ defined in Eq. (2.59) was eventually computed using a central finite difference:

$$\alpha(T) = \frac{1}{3V_0(T)} \frac{\partial V_0(T)}{\partial T} \approx \frac{1}{3V_0(T)} \frac{V_0(T + \delta T) - V_0(T - \delta T)}{2\delta T} \ . \tag{3.4}$$

A step size of $\Delta T = 5K$ was chosen to ensure the stability of the finite difference; with respect to the computational parameters for the DFT and phonon calculations, the converged settings discussed in the previous sections were used.

The plots in Fig. (3.8) show both the temperature dependent equilibrium volume $V_0(T)$ and the thermal expansion $\alpha(T)$ of Mg_2Si computed with different XC-functionals. Again,
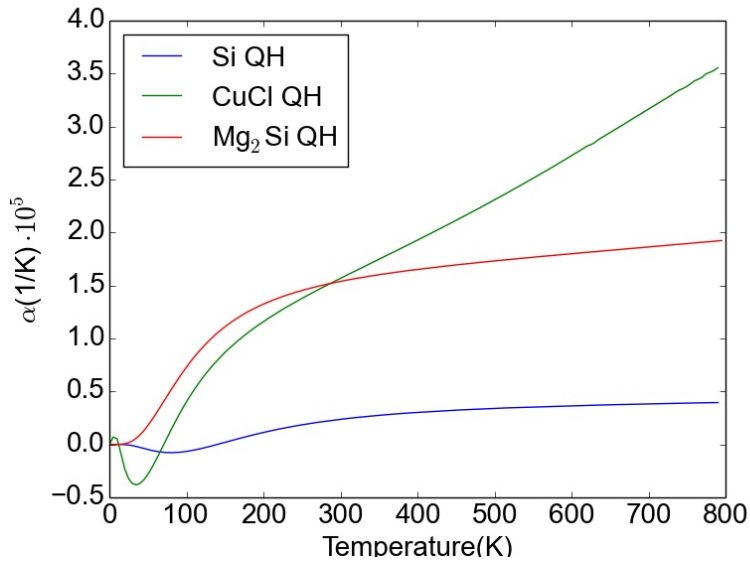
Figure 3.9: Thermal expansion coefficient $\alpha(T)$ computed in the quasi-harmonic approximation using DFT-PBEsol for Si, CuCl, and Mg2Si. The chosen computational settings for Si and CuCl can be found in Appendix 7.

we find only a week dependence of these properties of Mg_2Si on the chosen XC functional. Again, PBE exhibits the highest lattice expansion and LDA the lowest due to their "under/overbinding" discussed before. To a very large extent, this dependence has its roots in the too large/too small volume found already in the static limit (see Sec. 3.1), as can be seen from the fact that the temperature dependent equilibrium volumes $V_0(T)$ differ essentially by a constant offset. Accordingly, the lattice expansion $\alpha(T)$ for the different functionals are almost indistinguishable.

To better classify Mg_2Si, it is again useful to compare its thermal expansion coefficient $\alpha(T)$ with the one of Si and CuCl, two materials known for their strong harmonicity/anharmonicity. As shown in Fig. 3.9, Mg_2Si exhibits a strong lattice expansion, given that its room temperature value of $\alpha(300K) = 1.55$ 1/K is almost the same as the one of CuCl ($1.57 \cdot 10^{-5}$ 1/K) and thus 6.6 times larger than the one of silicon ($2.37 \cdot 10^{-6}$ 1/K). Also, it is important to note that the thermal expansion of Mg_2Si is always positive ($\alpha(T) > 0$). Conversely, a negative lattice expansion is observed at low temperatures in the case of silicon and CuCl (see Fig. 3.9). This effect is typical for zinc blende and diamond structures; a detailed discussion [20] would however go beyond the scope of this work.

Interestingly, the harmonic properties of Mg_2Si discussed in the previous section suggested that Mg_2Si should behave qualitatively similar to Si. The *quasi-harmonic calculations* in this section, however, suggest that the anharmonic effects probed by these approach are in the same order of magnitude as the ones found in CuCl. This –as well as the roots of the strong lattice expansion in Mg_2Si– can be understood in detail by investigating its total overall Grüneisen parameter $\gamma(T)$ defined in Eq. (2.62). In the following, three different approaches where used to compute $\gamma(T)$ and the associated thermal expansion $\alpha(T)$ to

disentangle the different contributions to this effect:

(QH): Using the relation given in Eq. (2.60) for the lattice expansion $\alpha(T)$, we can compute the overall Grüneisen parameter $\gamma(T)$ using

$$\gamma(T) = \frac{3\alpha(T)B_0(V_0(T))}{C_V(T)} \tag{3.5}$$

directly from the outcome of the *quasi-harmonic* calculations discussed before. Given that the quantities entering this expression were computed by explicitly investigating different volumes V_0^i, the dependence on the volume is inherently taken into account, e.g., by using the temperature dependent bulk modulus $B_0(V_0(T))$.

(FD): In this approach, the overall Grüneisen parameter $\gamma(T)$ is computed from the *mode-specific* Grüneisen parameters $\gamma_s(\mathbf{q})$ using Eq. (2.62). The required *mode-specific* Grüneisen parameters $\gamma_s(\mathbf{q})$ are calculated from the volume derivative of the dynamical matrix $D(\mathbf{q})$ as detailed in Eq. (2.63). The latter derivative is performed using a centered finite difference approaches, see Eq. (2.64), which requires three individual phonon calculations for the volumes $V, V + \delta V, V - \delta V$ ($\delta V = 0.01V$). From the thereby determined overall Grüneisen parameter $\gamma(T)$, the lattice expansion $\alpha(T)$ is then computed using Eq. (2.60). It is important to note that all quantities in this approach are calculated at (or ΔV around) the equilibrium volume in the static limit. Accordingly, the temperature dependence of the bulk modulus B_0 is not accounted for.

(3rd): Conceptually, this approach is almost identical to the finite difference one (**FD**). The only difference is that in this case the *mode-specific* Grüneisen parameters $\gamma_s(\mathbf{q})$ are not determined via finite differences, but from third order harmonic force constants $\Psi_{IJK}^{\alpha\beta\gamma}$ using the perturbative expressions given in Eq. (2.74) and (2.75). Thereby, the third order harmonic force constants $\Psi_{IJK}^{\alpha\beta\gamma}$ are computed using the finite difference approach implemented in *phono3py* [26] and discussed for Eq. (3.3).

The plots in Fig. (3.10) show both the thermal expansion coefficients $\alpha(T)$ and the *overall* Grüneisenparameter $\gamma(T)$ for Mg$_2$Si, diamond Silicon, and zincblend CuCl as computed by the three techniques (**QH**, **FD**, and **3rd**) introduced above. As can be seen in Fig. (3.10), the three techniques generally yield results that agree with each other qualitatively. On a quantitative level, however, interesting differences arise that allow for direct insights on the degree anharmonicity. For this reason, for instance, the computed thermal expansion coefficient $\alpha(T)$ and the *overall* Grüneisen parameter $\gamma(T)$ are in good agreement for all three approaches in the case of Si, which is known to be particularly harmonic. For the more anharmonic Mg$_2$Si, the overall Grüneisenparameter $\gamma(T)$ is in good agreement for all three approaches, but the thermal expansion coefficients $\alpha(T)$ computed in the *quasi-harmonic approximation* (**QH**) deviates from the ones computed with **FD** and **3rd**. The reason for this deviation can be traced back to the fact that only the **QH** approach accounts for a temperature/volume dependent bulk modulus $B_0(V(T))$ in Eq. (3.5), whereas the **FD** and
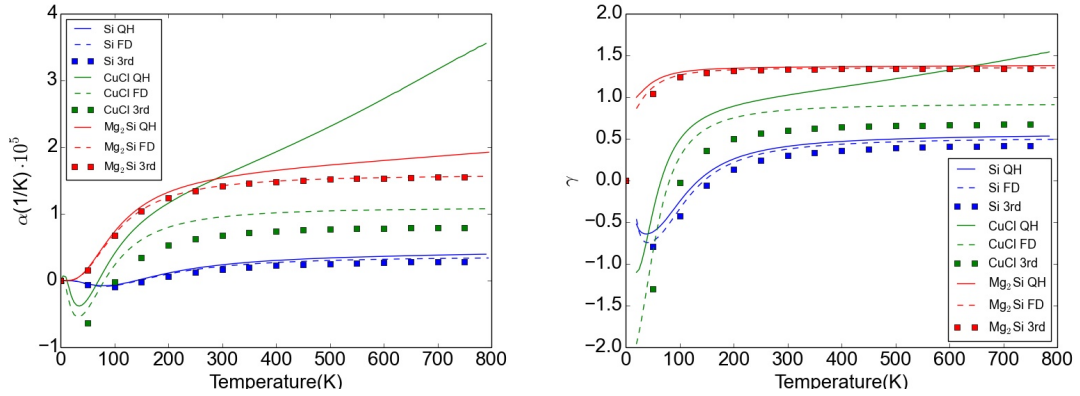
Figure 3.10: Thermal expansion coefficient $\alpha(T)$ (left) and *overall* Grüneisen parameter $\gamma(T)$ (right) of Mg$_2$Si, diamond Silicon, and zincblend CuCl calculated with DFT-PBEsol from three different approaches (**QH**, **FD**, and **3rd**; see text)

.

3rd approaches rely on the bulk modulus B_0 in the static limit. Even more prominently, this behaviour is observed for CuCl: In this case, it is not only the thermal expansion coefficient $\alpha(T)$ that differs between the methods due to the different treatment of the bulk modulus, but also the overall Grüneisenparameter $\gamma(T)$ differs: These results suggest that for this particular material, which is known for its anharmonicity, a perturbational, first order treatment in terms of finite differences close to equilibrium (**FD**) or third order force constants (**3rd**) is generally inappropriate, given that these approaches differ significantly from the quasi-harmonic approach (**QH**), in which also higher orders of anharmonicity are effectively incorporated.

It is important to note that the lattice expansion also introduces a temperature dependence in the phonon frequencies, given that these $\omega_s(\mathbf{q}, V(T))$ implicitly depend on the volume $V(T)$ in the quasi-harmonic approximation. Exemplarily, this is shown in Fig. 3.11 for Mg$_2$Si: Upon lattice expansion, the bonding and the interactions between the atoms decrease. Therefore, also the harmonic force constants and phonon frequencies are lowered. Given that the latter enter the entropic term in the harmonic free energy in Eq. (2.50), this is the reason that lattice expansion takes place at all when increasing the temperature. Still, the changes with temperature observed for Mg$_2$Si in Fig. 3.11 are rather minute, purely quantitative and not qualitative. In particular, the most siginificant changes occur in the high-frequency portion of the spectrum ($\omega > 6$ THz). Given that the phonon modes in this range are not particularly important for the thermal conductivity (see next section), lattice expansion has been neglected in these latter chapters.

3.2.4 Lattice Thermal Conductivity of Magnesium Silicide

As discussed in detail in Sec. 2.2.4 and 3.2.2, the lattice thermal conductivity κ can be computed in first order approximation by perturbatively treating the anharmonicity
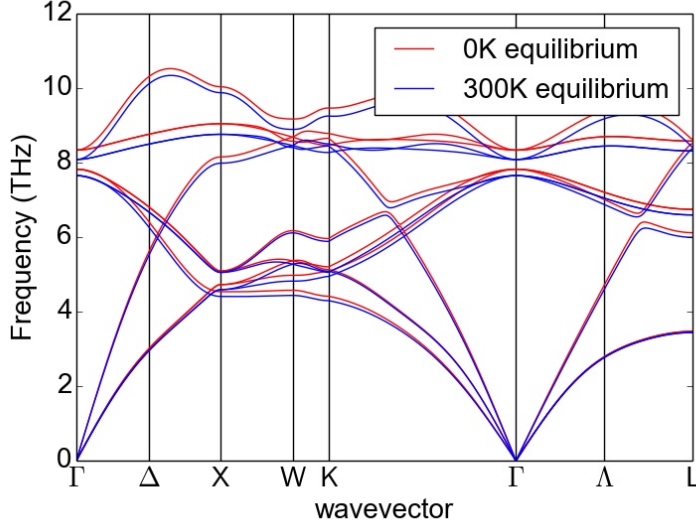
Figure 3.11: Phonon band structure of Mg_2Si for the lattice constant (6.33 Å) in the static limit (red: 0K equilibrium) and at the lattice constant (6.36 Å) predicted by the quasi-harmonic approximation at 300K (blue: 300K equilibrium). All calculations were performed using the PBEsol XC-functional.

using third order force constants $\Psi_{IJK}^{\alpha\beta\gamma}$, as defined in Eq. (2.66). For this purpose, the *phono3py* [26] code package was interfaced with the DFT code *FHI-aims* [33], as discussed in Sec. 3.2.1. By these means, the third order force constants $\Psi_{IJK}^{\alpha\beta\gamma}$ are determined via a finite difference approach using Eq. (3.3): Again, a $(2 \times 2 \times 2)$ cubic supercell was used for computing these third order force constants $\Psi_{IJK}^{\alpha\beta\gamma}$ in the case of Mg_2Si, given that the calculations and analysis presented in Sec. 3.2.1 showed that qualitative and quantitative results can be obtained by these means. Subsequently, a $(18 \times 18 \times 18)$ $\mathbf{q}$-grid was used to compute the Fourier transformed third order force constants $\Psi_{s,s',s''}(\mathbf{q}, \mathbf{q}', \mathbf{q}'')$ defined in Eq. (2.87) and then the lifetimes $\tau_s(\mathbf{q})$ using Eq (2.85) and (2.86). Consistently, the exact same supercell and $\mathbf{q}$-grid was used to in the respective harmonic calculations (see Sec. 3.2.2) to compute the phonon frequencies $\omega_s(\mathbf{q})$, group velocities $\mathbf{v}_s(\mathbf{q})$ using Eq. (2.48), and the *mode-specific* specific heats $c_s(\mathbf{q})$ defined in Eq. (2.51). Eventually, all these ingredients are combined to compute the diagonal entries of the thermal conductivity tensor using the expression

$$\kappa = \frac{1}{V_0} \sum_{\mathbf{q},s} c_s(\mathbf{q}) \mathbf{v}_s^2(\mathbf{q}) \tau_s(\mathbf{q}) \; . \tag{3.6}$$

already discussed in Sec. 2.2.4. Please note that due to the cubic symmetry of Mg_2Si, Si, and CuCl, all diagonal entries of the thermal conductivity tensor $\kappa = \kappa_{xx} = \kappa_{yy} = \kappa_{zz}$ are equal. To asses which modes contribute the most to the thermal conductivity and to qualitatively discuss the differences between different XC-functionals and/or materials, it is also useful
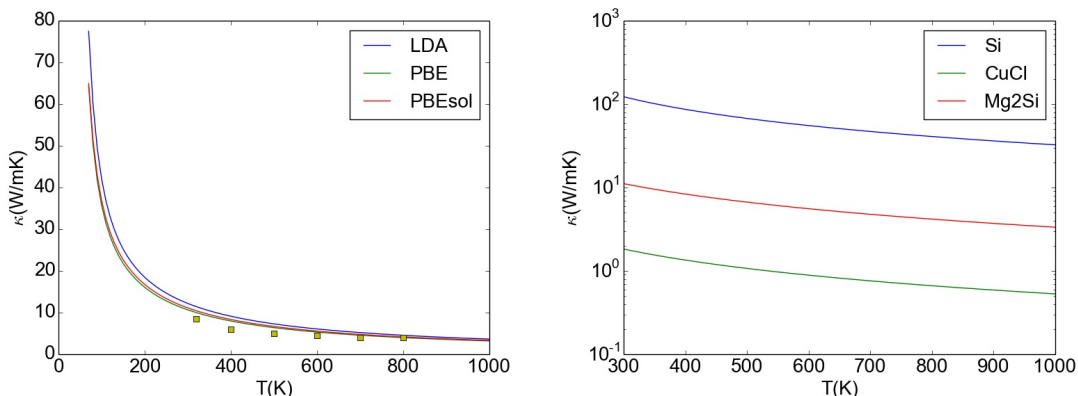
Figure 3.12: Computed lattice thermal conductivity κ: The left plot shows how the lattice thermal conductivity κ depends on the chosen XC-functional. The also shown experimental data (green squares) was taken from Ref. [54]. The right plot shows a comparison of the lattice thermal conductivities κ of Mg_2Si, Si, and CuCl, which were all computed with DFT-PBEsol.

to introduce the normalized density of the thermal conductivity

$$\kappa_{dos}(\omega) \quad = \quad \sum_s \int \left[c_s(\mathbf{q}) \tau_s(\mathbf{q}) |\mathbf{v}_s(\mathbf{q})|^2 \right] \delta(\omega - \omega_s(\mathbf{q})) d\mathbf{q} \,, \tag{3.7}$$

which quantifies the contributions to the thermal conductivity stemming from a specific frequency ω. In all cases, the converged computational settings (**k**-points, basis set, integration grids) discussed in the previous sections were used in the underlying DFT calculations.

Fig. 3.12 (left) shows the lattice thermal conductivities κ of Mg_2Si computed by these means using the LDA, PBE, and PBEsol XC-functionals. The agreement with the also shown experimental values [54] is satisfactory in all cases, given that also this property of Mg_2Si appears not to be particularly sensitive on the chosen XC functional, in line with the findings in the previous sections. To put this result into perspective, it is again useful to compare the computed thermal conductivity of Mg_2Si with the ones computed for silicon and CuCl (see Appendix 7 for the chosen computational settings). As also shown in Fig. 3.12 (right), the thermal conductivity of Mg_2Si lies between the one of the very anharmonic CuCl and the very harmonic Silicon: For instance, at 300K the thermal conductivity of Mg_2Si has as value of 11.125 (W/mK), whereas the one of Si is 122.53 (W/mK) and the one of CuCl is 1.828 (W/mK) (calculated with PBEsol).

The discussion of an integrated quantity such as κ is not particularly useful to disentangle the different contributions. For this reason, Fig. 3.13 (upper left) also shows the normalized density of the thermal conductivity $\kappa_{dos}(\omega)$ computed for Mg_2Si at 300K using different XC-functionals. Clearly, the dominant contribution (93%) to the thermal conductivity of Mg_2Si stems from the frequency range between approx. 1 and 8 THz. The respective
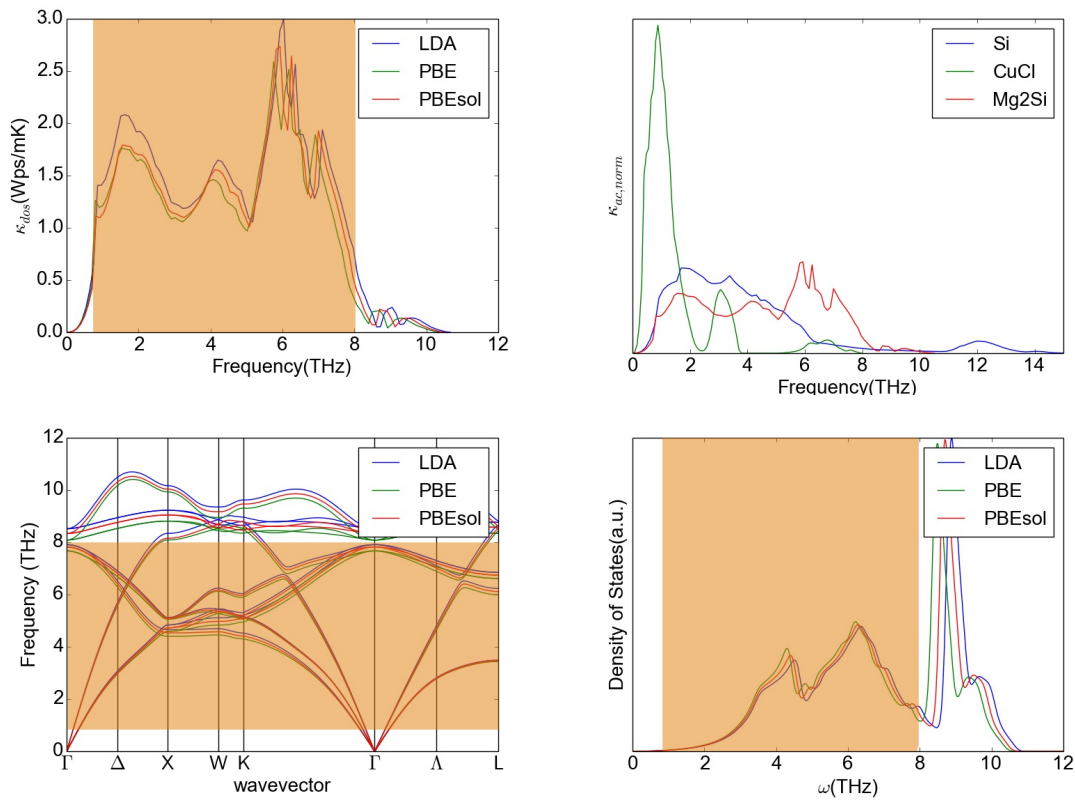
Figure 3.13: Thermal conductivity (left), density of the thermal conductivity (right) at 300K, phonon band structure (left below) and phonon density of states (right below) of Mg$_2$Si for LDA, PBE and PBEsol the orange are mark frequencies with the highest contribution to the thermal conductivity.
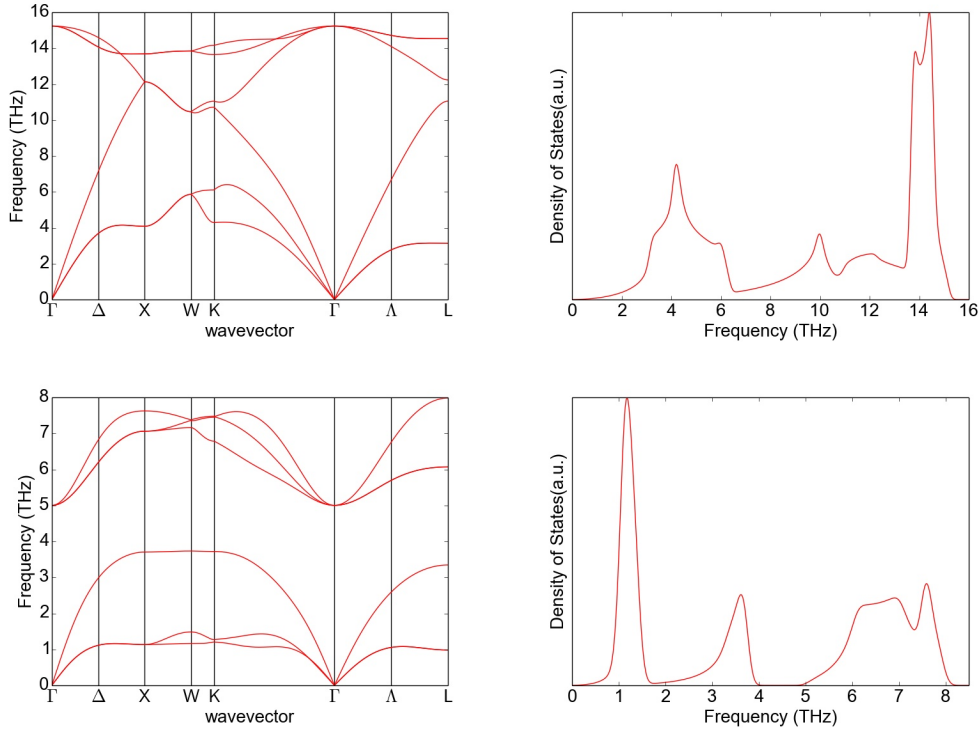
Figure 3.14: Phonon band structure and phonon density of states of Si (above). Phonon band structure and phonon density of states of CuCl (below)

band structure plot also shown in Fig. 3.13 (lower left) reveals that this is the region in which highly dispersive modes with large group velocities, especially acoustic modes, occur. Interestingly, modes in the range between 1 and 3 THz have a significant contribution of 26% to the thermal conductivity, in spite of the fact that the vibrational density of states (also shown in Fig. 3.13, lower right) in this range is actually almost negligible (only 3% of the total density of states). A more detailed discussion of the physical mechanisms driving this behaviour can be found later in this chapter, given that this requires to decompose and understand the contributions to thermal conductivity in more detail. For instance, this becomes clear from the fact that LDA has much larger contributions in the 1 to 3 THz frequency range than PBE and PBEsol, in spite of the fact that the respective band structures are virtually indistinguishable in this range. Still, all three functionals yield the same qualitative and almost the same quantitative results for the portion of $\kappa_{dos}(\omega)$ that contributes most to the thermal conductivity.

Furthermore, the normalized density of the thermal conductivity $\kappa_{dos}(\omega)$ is compared for three different systems (Mg_2Si, Si, CuCl) in Fig. 3.13 (upper right). Interestingly, this reveals that Mg_2Si behaves qualitatively different than both Si and CuCl: While most of the thermal conductivity of Mg_2Si stems from a wide range of modes between 1 and 8 THz, most of the thermal conductivity of Si and especially CuCl stems from lower frequency modes, i.e., from modes between 1 and 6 THz for Si and from modes below 4 THz in for CuCl. In part, this can be rationalized from the fact that by definition modes that

exhibit a vanishing dispersion $\mathbf{v}_s(\mathbf{q}) = \partial\omega_s(\mathbf{q})/\partial\mathbf{q} \approx 0$ cannot contribute to the thermal conductivity by definition, see Eq. (3.6). In part, this is the reason that the high-frequency optical modes with high density of states, i.e., the peak at 9 THz for Mg_2Si and the peak at 14 THz for Si, have negligible contributions to κ. Similarly, this is in part the reason that the low frequency acoustic modes with high group velocities $\mathbf{v}_s(\mathbf{q})$ contribute much more to κ than the respective density of states would suggest. However, this kind of analysis is not sufficient to qualitatively and quantitatively explain all the features of $\kappa_{dos}(\omega)$, as will become even clearer in the next section. For instance, the high-frequency modes of CuCl in the range between 5 and 8 THz exhibit a notable dispersion $\mathbf{v}_s(\mathbf{q})$, but have no significant contribututions to κ.

3.3 Approximative Treatment of the Anharmonicity

As discussed in Sec. (3.2.1), the computational effort required to determine the third order force constants is significant, in particular for systems with low degrees of symmetry, e.g., when an impurity atom breaks the symmetry. For this reason, the cost of a computational high-throughput screening of the lattice thermal conductivity is in many cases prohibitive. Various approximations (see Sec. 3.3) have been proposed to estimate the lattice thermal conductivity so that such studies can be performed nonetheless. However, the validity and accuracy of these approximations is still topic of scientific debate, as already substantiated by the fact that so many conceptually different approximations have been proposed. For this reason, these approximations are investigated for Mg_2Si, Si, and CuCl in this section and compared to the results of a full lattice thermal conductivity calculation. This allows to analysis and discuss the applicability and limits of these approximations.
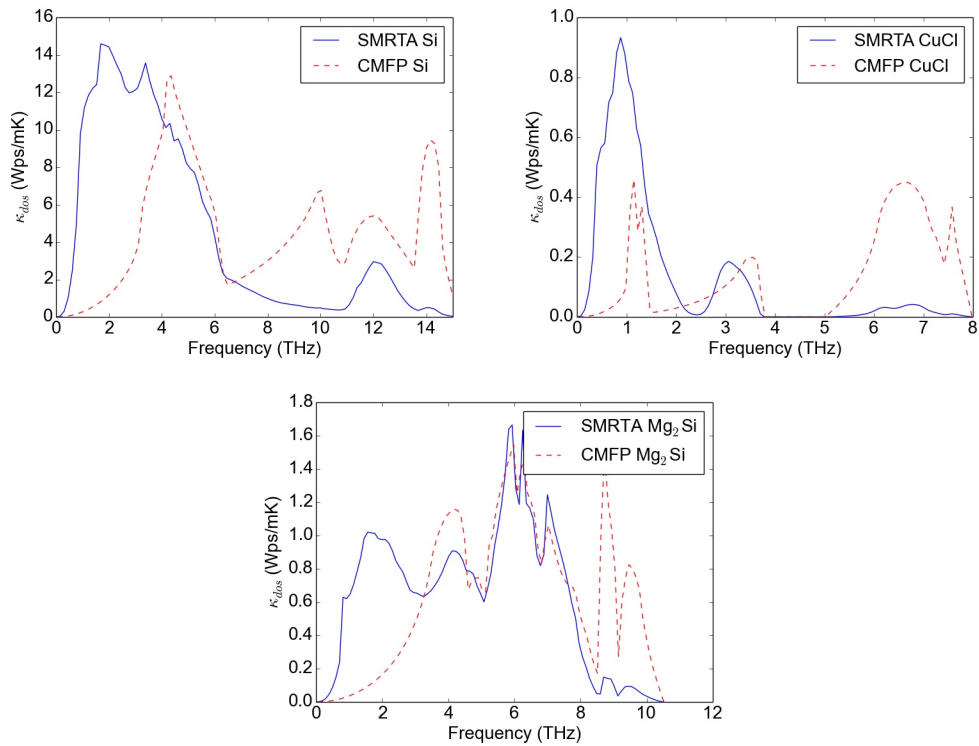
Constant Mean free Path Approximation: In the *constant mean free path approximation* (CMFP) as defined in Eq. (2.91) the mean free path (product of group velocity and lifetime) is assumed to be a mode-independent parameter Λ that can be estimated. In our case, we have chosen Λ in such a way that the respective thermal conductivity in the *single mode relaxation time approximation* (SMRTA) is reproduced exactly. To analyze if this is a meaningful approximation, we compare the respective density of the thermal conductivity between the SMRTA and the CMFP, as shown in Fig. 3.16. This allows to understand if the correct physical contributions to the conductivity are reproduced by the approximation.

In all cases shown in Fig. (3.16), the CMFP overestimates contributions in the high-frequency range and underestimates the contributions in the low-frequency range. In some cases, the locations of peaks is correctly reproduced. Their relative height is however generally incorrect. In spite of its quite wide-spread application [41], this thus not appear to be a valid and trustworthy physical model. To asses how the CMFP method performs at
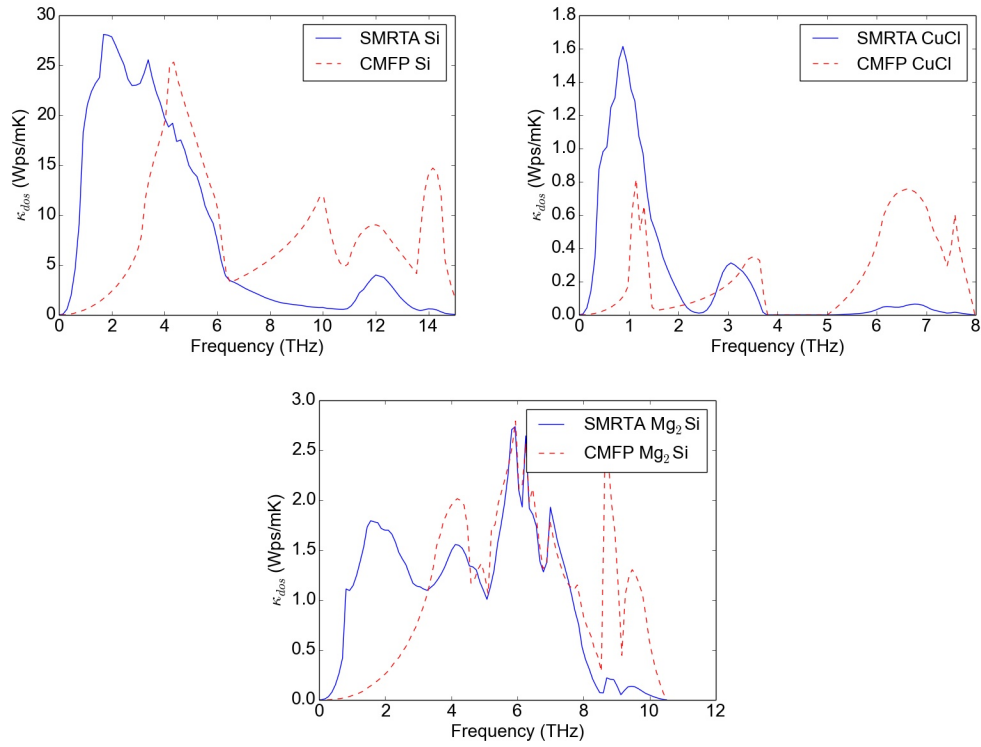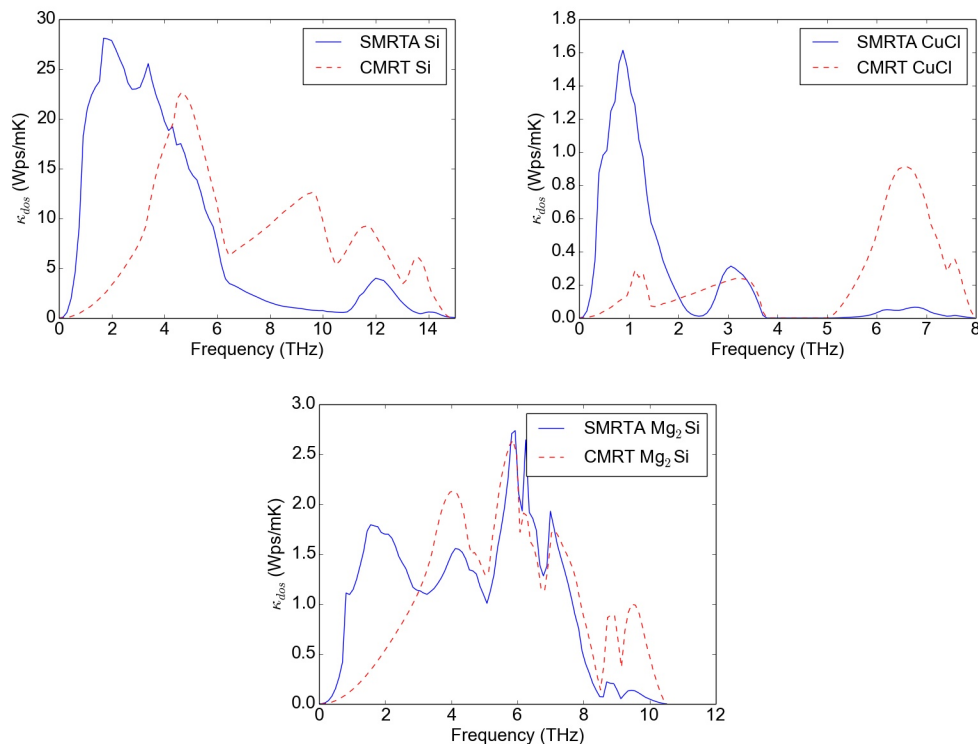
Figure 3.15: Density of the thermal conductivity of Si (left), CuCl, and Mg_2Si (below) in the *single mode relaxation time approximation* (SMRTA) and the *constant mean free path approximation* (CMFP) at 300K. In the latter case, the parametric mean free path Λ was chosen in such a way that the SMRTA thermal conductivity is reproduced exactly.
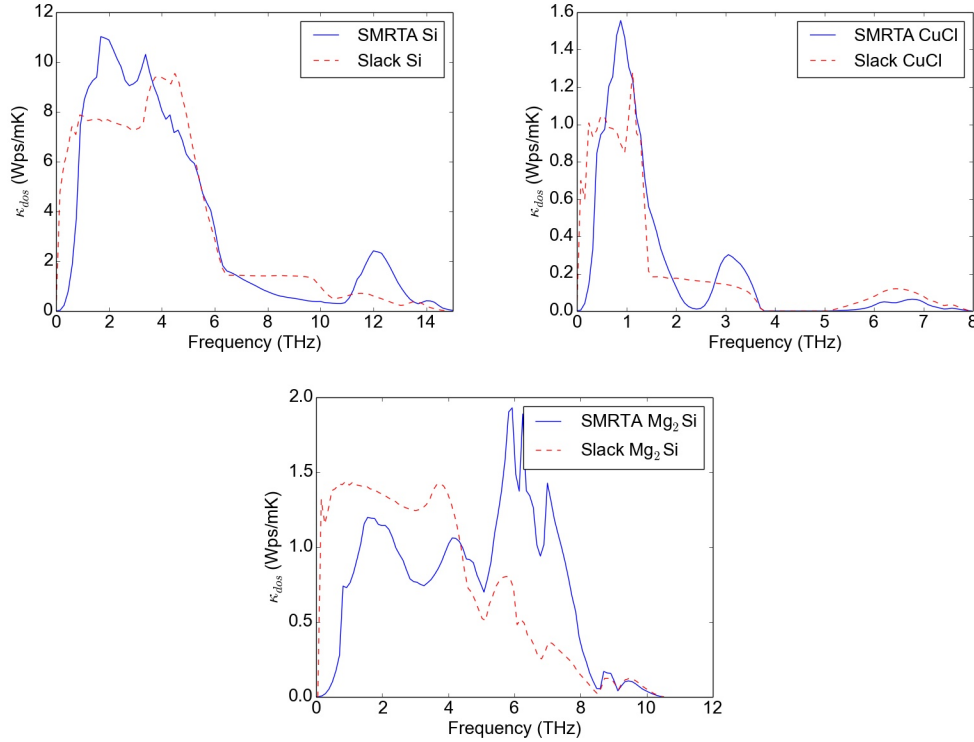
Figure 3.16: Density of the thermal conductivity of Si (left), CuCl, and Mg$_2$Si (below) in the *single mode relaxation time approximation* (SMRTA) and the *constant mean free path approximation* (CMFP) at 500K. In the latter case, the parametric mean free path Λ was chosen in such a way that the SMRTA thermal conductivity is reproduced exactly.

Figure 3.17: Density of the thermal conductivity of Si (left), CuCl, and Mg$_2$Si (below) in the smrta (single mode relaxation time approximation) and CMRT (constant mean relaxation time approximation) at 300K.

different temperatures, Λ was now chosen to reproduce exactly the results of the SMRTA at a temperature of 500K. As can be seen the qualitative results in both the SMRTA method and the CMFP method remain largely the same.

Constant Relaxation Time Approximation: The *constant mean relaxation time approximation* (CMRT) is conceptually similar to the CMFP approximation discussed above, see Sec. 2.2.4. In this case, however, a constant relaxation time τ is assumed, which in turn leads to a **quadratic** dependence of the thermal conductivity density on the group velocities. Again, the parameter τ needs to be estimated. In this work, it was again chosen in such a way that the respective thermal conductivity in the *single mode relaxation time approximation* (SMRTA) is reproduced exactly. As shown in Fig. 3.17, similar trends as in the case of the CMFP approximation are observed: Again, high-frequency contributions are generally overestimated, whereas low-frequency contributions are underestimated. In part, this erroneous trend is even more severe than in the CMFP case, given that group velocities now enter quadratically: This is for instance the case for CuCl, for which the contributions from high frequency phonons are even more overestimated, while the contributions from low frequency phonons are even more underestimated.

Figure 3.18: Density of the thermal conductivity of Si (left), CuCl, and Mg$_2$Si (below) in the smrta (single mode relaxation time approximation) and Slack's approximated lifetime at 640K (Si), 310K (CuCl), and 430K (Mg$_2$Si).

Slack's Lifetime In the last discussed approximation, the expressions for the thermal conductivity κ and $\kappa_{DOS}(\omega)$ given in Eq. (3.6) and (3.7) are fully evaluated. However, the lifetime $\tau_s(\mathbf{q})$ is approximated by an analytic, frequency-dependent expression given in Eq. (2.89). This approximation was proposed by Slack and Galginaitis in 1964 [39] on the basis of empirical findings for temperatures close to the Debye temperature of the material using a simple Debye model. For the more complex phonon band structures of interest in this work, the Debye temperature $\Theta_D(\infty)$ is determined using the second moment of the density of states $g(\omega)$ [40]:

$$\Theta_D(\infty) = 2\pi \frac{\hbar}{k_b} \sqrt{\frac{\int_0^\infty \omega^2 g(\omega)d\omega}{\int_0^\infty g(\omega)d\omega}} \ . \tag{3.8}$$

Still an empirical parameter p, which needs to be estimated, is required; again, it was chosen in this work in such a way that the respective thermal conductivity in the *single mode relaxation time approximation* (SMRTA) is reproduced exactly. As shown in Fig. 3.18, this approximation performs considerably better than the CMFP and the CRT approximations due to the fact that in this case the lifetimes are not frequency-independent, but scale with $\omega_s^{-2}(\mathbf{q})$. Inherently, this captures the fact that contribution to κ stemming from low frequency modes is much stronger than the one of high frequency modes, and thus improves on the CMFP and the CRT. Although this approximations yields much more
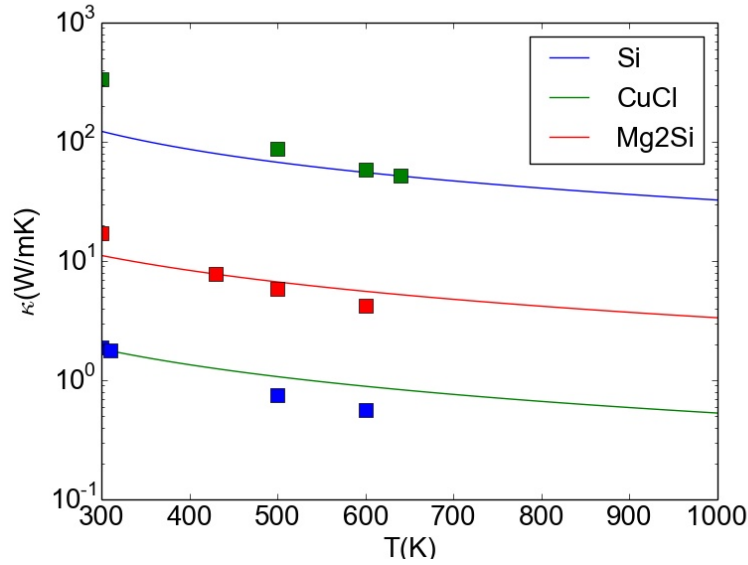
Figure 3.19: The plot shows the comparison of how Slack's approximation performs at different temperatures for CuCl (p estimated at 310K), Si (p estimated at 640K), and Mg$_2$Si (p estimated at 430K)

reasonable results for $\kappa_{DOS}(\omega)$, the agreement with a full SMRTA calculation is far from perfect: The very low-frequency region is generally overestimated due to the divergence of the $\omega_s^{-2}(\mathbf{q})$ term close to zero. In turn, contributions from highly-dispersive optical modes are underestimated, e.g., in Si for frequencies around 12 THz and even more severely for Mg$_2$Si for frequencies around 6 THz. Since Slack's approximation also depends on the temperature it allows for an estimate away from the temperature at which the parameter p was estimated. As observed in Fig. 3.19 Slack's model yields good resuls near the temperatures at which the parameter p was estimated. However the thermal conductivity can be massively overestimated if it is too far away from the temperature p was estimated at. In case of Si for example the thermal conductivity at 300K is overestimated by c.a. a factor of 3.

4 Properties of Doped Magnesium Silicide

4.1 Methodology & Chosen Impurities

As discussed in Sec. 3, Mg_2Si has recently attracted scientific interest due to its promising thermoelectric properties. In this context, also extenstive research on doped Mg_2Si was published:

On the Si site [56, 57, 58]

On the Mg site [55]

Inspired by this mostly experimental studies, we compiled a list of possible substitutional dopants that covers the impurities discussed in literature (see Fig. 4.1) and to extent the list to cover a large portion of chemical space in a systematic fashion. For the substitution of Si, we have investigated impurities in row 4, 5, and 6 and group 12-16; for the substitution of Mg, row 3, 4, and 5 and group 1 and 2 were investigated (see Fig. 4.1). With respect to impurity concentrations, we have limited ourselves to 3.13% doping for Si substitution and 1.56% doping for Mg substitution. This corresponds to substituting exactly one atom in a 96-atom, $2 \times 2 \times 2$ conventional cubic Mg_2Si supercell (32 fcc unit cells). In these supercells sizes, the harmonic and anharmonic properties are correctly reproduced, as discussed in Sec. 3.2.1.

For each of these compositions, equilibrium lattice constants a_0, bulk moduli B_0, and its derivatives B_0' were determined by fitting to the Birch-Murnaghan equation using the exact same procedure already discussed in Sec 3.1. By calculating the effective stress in the thereby determined equilibrium structure, we were able to check that the cubic symmetry is indeed retained upon relaxation. Eventually, phonon calculations were performed in this doped ($2 \times 2 \times 2$) cell. The same numerical settings used for Mg_2Si were employed in these calculations as well (same $\mathbf{k}$-point density in the respective Brillouin zones, "tight" integration grids, the basis sets used for Mg and Si before, and a "tier 1" basis set for the dopants.)

To qualitatively analyse the effect of dopants on the vibrational properties, the phonon densities of states $g(\omega)$ defined in Eq. (2.54) were computed. In addition, also the analogously defined averaged group velocities $\bar{v}(\omega)$ and mode heat capacities $\bar{c}(\omega)$ were ana-
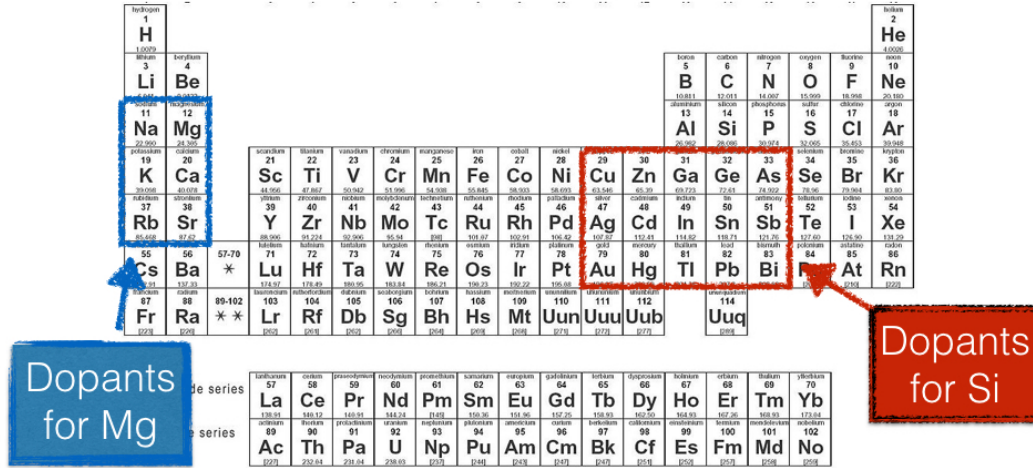
Figure 4.1: Chosen Dopands:

lyzed:

$$\bar{v}(\omega) = \sum_s \frac{\int_0^\omega |\mathbf{v}(\mathbf{q}, s)| \delta(\omega - \omega(\mathbf{q}, s)) d\mathbf{q}}{\int_0^\omega \delta(\omega - \omega(\mathbf{q}, s)) d\mathbf{q}} \tag{4.1}$$

$$\bar{c}(\omega) = \sum_s \frac{\int_0^\omega c_{\mathbf{q}, s} \delta(\omega - \omega(\mathbf{q}, s)) d\mathbf{q}}{\int_0^\omega \delta(\omega - \omega(\mathbf{q}, s)) d\mathbf{q}} \ . \tag{4.2}$$

4.2 Effect of Substitutional Doping on Silicon Sites

In Tab. 4.1, the volume V_0, bulkmodulus B_0, and pressure derivative of the bulkmodulus B_0' are listed for a representative selection of the investigated dopants on substitutional Si sites. Generally, the effect of doping on the Si sites has almost negligible effects on these quantities: In comparison to pristine Mg_2Si, the volume slightly expands, whereas the bulk modulus retains its value. The pressure derivative of the bulk modulus B_0' decreases quite significantly. However, also this decrease is essentially independent of the chosen dopant.

The computed vibrational density of states for different dopants is compared in Fig. 4.2 to the one of pristine Mg_2Si. At first sight, the effects of doping appear to be minute; still, some important qualitative trends can be observed: Generally, the intensity of the high-frequency peak at 9 THz is reduced by doping. This is consistent with the slightly larger volume observed upon doping (see Tab. 4.1), which is expected to lower the optical frequencies (see Fig. 3.11 and its discussion). Additionally, a low-frequency peak becomes visible for heavier dopants such as Ag, Sn, Au, or Bi at around 2 THz. This peak is associated to an optical, localized mode of the defect; its frequency is thus essentially
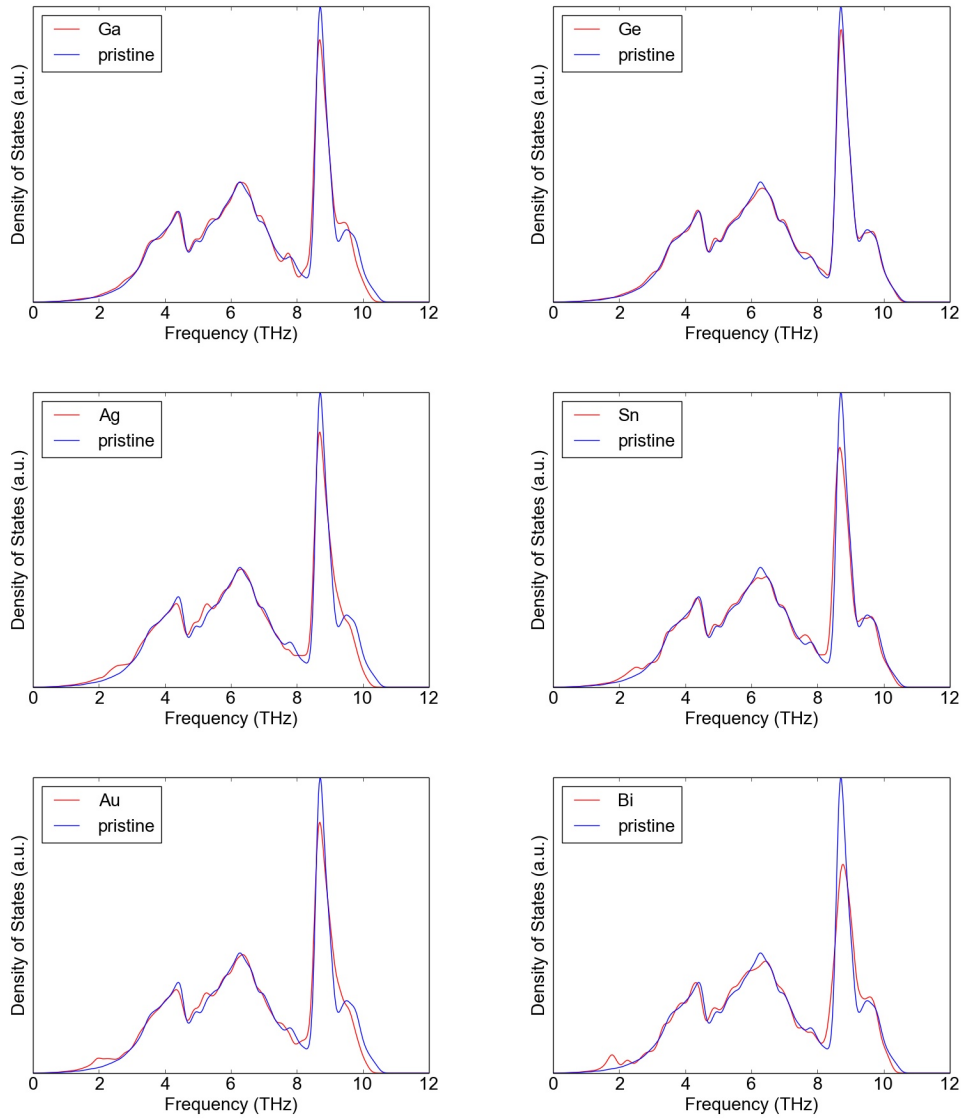
Figure 4.2: Mg$_2$Si: Phonon density of states for substitutional doping on the Si site with Ga, Ge, Ag, Sn, Au and Bi dopants in comparison with pristine Mg$_2$Si.

	Substitution on the Si Site				Substitution on the Mg Site		
	V_0 (Å^3)	B_0 (eV/Å^3)	B_0'		V_0 (Å^3)	B_0 (eV/Å^3)	B_0'
Pristine Mg$_2$Si	2028	0.35	3.91	Pristine Mg$_2$Si	2028	0.35	3.91
Ga	2032	0.35	3.51	Na	2035	0.34	3.51
Ge	2029	0.35	3.51	K	2049	0.34	3.51
Ag	2033	0.34	3.51	Ca	2056	0.34	3.51
Sn	2041	0.35	3.51	Rb	2056	0.34	3.51
Au	2031	0.35	3.51	Sr	2050	0.34	3.51
Hg	2037	0.35	3.51	-	-	-	-
Bi	2042	0.34	3.51	-	-	-	-

Table 4.1: Doped Mg$_2$Si: Equilibrium volume V_0, the bulk modulus B_0, and its derivative B_0' as determined by Birch-Murnaghan fits to DFT data computed with the PBEsol XC-functionals. For substitution on the Si site, only a representative selection of dopants is listed, whereas all investigated substitutional dopants for the Mg site are given.

inversely proportional to the mass of the dopant. As can be examplarily seen from phonon band structure of Ag doped Mg$_2$Si shown in Fig. 4.3, this optical modes crosses the original acoustic phonon modes of the pristine Mg$_2$Si crystal.

Although the impact of the dopants on the density of state is almost negligible, its influence on the thermal conductivity is not, as will be detailed quantitatively in the next section. This can already be expected from the fact that the group velocities are quite strongly altered by the dopants: As shown in Fig. 4.4, the averaged group velocity $\bar{v}(\omega)$ generally decreases over the whole range of frequencies and in particular in the range between 3 and 8 THz that contributes significantly to the thermal conductivity of Mg$_2$Si (see Sec. 3.2.4). Again, this can be rationalized by inspecting the respective phonon band structures: As shown exemplarily for Ag doped Mg$_2$Si in Fig. 4.3, the backfolding of the Brillouin zone in this extended unit cell and the occurring break of symmetry due to the dopant induces a quite dense, almost dispersionless phonon band structure in this frequency range and thus the reduction in $\bar{v}(\omega)$. For frequencies below 3 THz, which significantly contribute to thermal conductivity as well, the reduction in $\bar{v}(\omega)$ is purely caused by the localized optical mode of the defect. This mode significantly disrupts the dispersion and reduces the group velocities of the original acoustic phonon modes of the pristine Mg$_2$Si crystal.

Conversely, the averaged mode heat capacities $\bar{c}(\omega)$ also shown in Fig. 4.4 are hardly affected by doping: In the classical limit of Dulong-Petit ($c_V = 3Nk_B$), this is self-evident, since the substitutional doping does not alter the number of atoms N. But even at temperatures below the Debye temperature, no significant influence is observed.
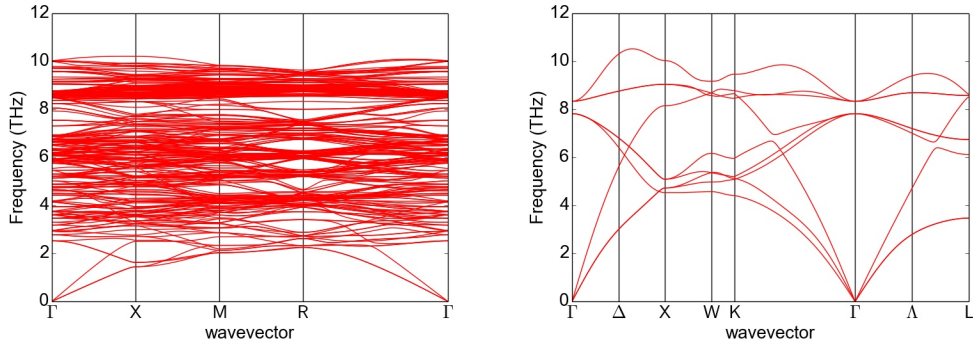
Figure 4.3: Left: Phonon band structure of Ag doped Mg_2Si (Si substitution, PBEsol XC-functional). Given that the unit cell for this defected system contains 96 atom ($2 \times 2 \times 2$ supercell of pristine Mg_2Si), the original Brillouin zone of Mg_2Si is backfolded, so that one gets a total of 288 phonon modes per **q**-point. Right: The respective phonon band structure of pristine Mg_2Si is shown for comparison.
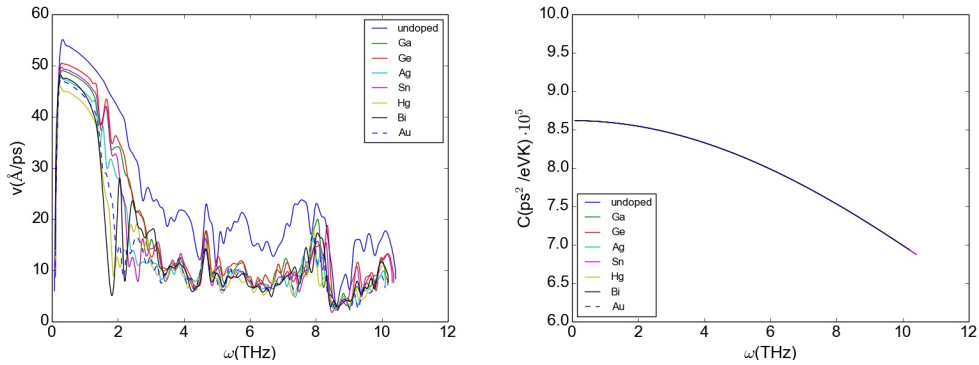
Figure 4.4: Mg_2Si: Averaged phonon group velocity $\bar{v}(\omega)$ (left) and averaged mode heat capacity $\bar{c}(\omega)$ (right) at 300K for substitutional doping on the Si site with Ga, Ge, Ag, Sn, Au, Hg, and Bi dopants in comparison with pristine Mg_2Si.
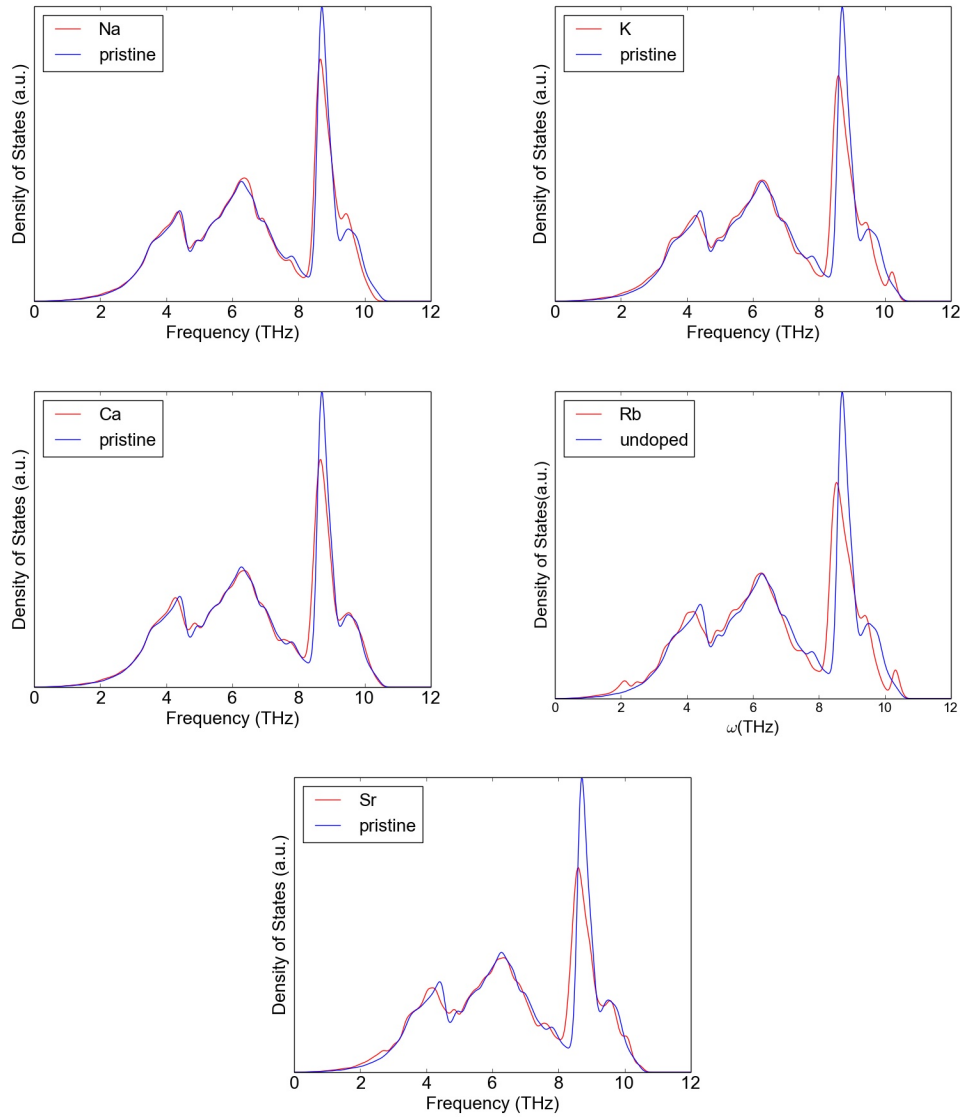
Figure 4.5: Phonon Desity of States of Na, K, Ca, Rb and Sr doped Mg_2Si in comparison with pristine Mg_2Si

4.3 Effect of Substitutional Doping on Magnesium Sites

In Tab. 4.1 the volume V_0, bulk modulus B_0, and its pressure derivative B_0' are listed for the investigated dopants on substitutional Mg sites. Qualitatively, the same trends as for Si substitution are seen. The volume expands, the bulk modulus is retained, and its derivative is decreased quite significantly regardless of the dopant's species. Quantitatively, however, the trends in volume expansion are stronger for Mg substitution.

In Fig. 4.5, the computed vibrational density of states is again compared to the one of pristine Mg_2Si. Again the effects of substitution on the Mg site seem to be more pronounced in comparison to substitution on the Si site. For heavier dopants, a significant decrease in the height of the peak at 9 THz is observed as well as a slight shift to lower frequencies.
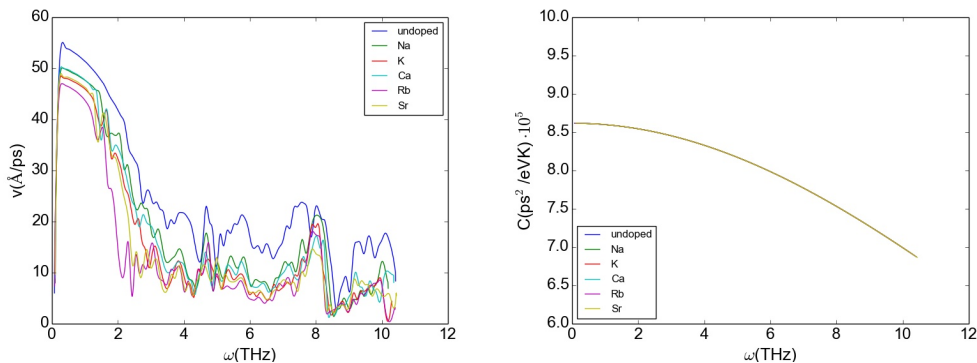
Figure 4.6: Mg$_2$Si: Averaged phonon group velocity $\bar{v}(\omega)$ (left) and averaged mode heat capacity $\bar{c}(\omega)$ (right) at 300K for substitutional doping on the Mg site with Na, K, Ca, Rb and Sr dopants in comparison with pristine Mg$_2$Si.

The latter has its roots in the increased lattice expansion, as discussed in Sec. 3.2.3 (see Fig. 3.11 and respective text).

As in the case of substitution of the Si site, the influence on doping on the thermal conductivity can be expected to be more significant than the densities of states shown in Fig. 4.5 suggest. As shown in Fig. 4.6, the averaged group velocity $\bar{v}(\omega)$ decreases over the whole frequency range and especially for frequencies above 3 THz for the exact same reasons already discussed for substitution on the Si site. Again, no changes in the averaged mode heat capacity $\bar{c}(\omega)$ are observed (also see Fig. 4.6).

4.4 Estimating the Impact of Substitutional Doping on the Lattice Thermal Conductivity of Magnesium Silicide

As already discussed in Sec. 3.2.1, calculating the lattice thermal conductivity from first principles within the *single mode relaxation time* approximation (SMRTA) can easily become computationally extremely expensive, given that for a material with N atoms in the unit cell the $3N \times 3N \times 3N$ elements of the third order force constant matrix need to be computed. In particular, this is the case for systems with a large number of atoms in the unit cell and few symmetries, such as the substitutionally doped magnesium silicides discussed in this section: Indeed, a single lattice thermal conductivity calculation for one such doped system would require at least 14,000 DFT force evaluations and is thus at least 50 times more expensive than a calculation for pristine Mg$_2$Si. Even with very generous computational allocations, an extensive high-throughput study of such defected materials with dopants chosen across the periodic table is thus essentially unfeasible. For this exact reason, approximations to the SMRTA are needed to at least estimate the thermal conductivity of such doped materials in a computationally rapid way. Various approximations in this spirit have been proposed in literature: The theoretical
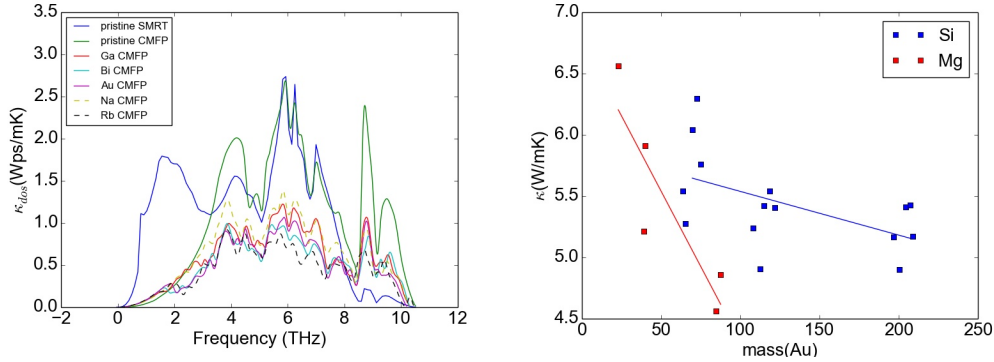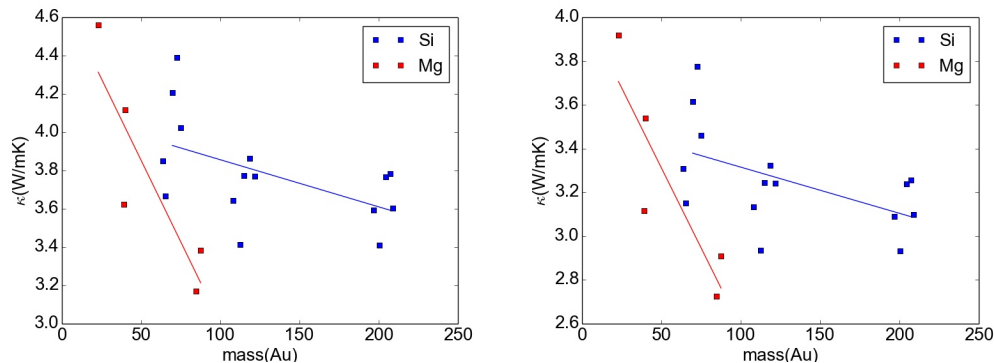
Figure 4.7: Constant mean free path approximation (CMFP) for substitutionally doped Mg$_2$Si: The left plot shows the density of the thermal conductivity $\kappa_{dos}(\omega)$ for selected substitutional doping on the Si (Ga, Bi, Au) and the Mg (Na,Rb) site. The right plot shows the estimated thermal conductivity at 300K plotted against the atomic mass of the dopant for all investigated substitutions.

concepts underlying these approximations were already discussed in detail in Sec. 2.2.4, the aspects regarding their practical application in Sec. 3.3. In this section, we thus limit ourselves to evaluate these approximations for the doped magnesium silicides discussed above.

4.4.1 Constant Mean Free Path Approximation

In the *constant mean free path* approximation (CMFP), the lattice thermal conductivity κ and the density of the thermal conductivity $\kappa_{dos}(\omega)$ were estimated by evaluating Eq. (3.7) for all doped magnesium silicides. The value for the required parameteric mean free path Λ at a temperature of 300K was chosen to be 52Å, i.e., the value for which CMFP and SMRTA calculations yield the exact same value of κ at this temperature (see Sec. 3.3) for pristine Mg$_2$Si. This implies the assumption that Λ is only marginally affected by doping, so that the value valid for pristine Mg$_2$Si can also be used for the doped compounds.

In Fig. 4.7, the density of the thermal conductivity $\kappa_{dos}(\omega)$ computed with the CMFP approximation for the doped silicides is compared to the one of pristine Mg$_2$Si (both CMFP and full SMRTA) is shown. For all investigated dopants, a distinct reduction of the $\kappa_{dos}(\omega)$ for all modes with frequencies larger than 2 THz is observed, which is consistent with the reduction observed for the average group velocities before (see Fig. 4.4 and 4.6). Here it is important to note that the CMFP severely underestimates contributions in the low frequency regime (see Fig. 4.7 and Sec. 3.3): Accordingly, it remains questionable if the CMFP is able to capture the influence of the localized optical mode that occurs for heavier defects in this frequency range and that can be expected to disrupts the transport contributions of the acoustic modes. Nonetheless, this approximation predicts that the

Figure 4.8: Thermal conductivities estimated in the constant mean free path approximation (CMFP) for substitutionally doped Mg_2Si as function of the dopants' mass (left: 430K, right: 500K).

thermal conductivity should decrease massively upon doping, e.g., by a factor of 1.70 for Na and 2.47 for Rb. As can be seen in Fig. 4.7, the CMFP predicts that heavier dopants are more effective in lowering the thermal conductivity. Also, substitution on Mg sites is more effective than substitution on Si sites, given that substitution Mg sites generally leads to a higher volume and thus to lower frequencies (see Sec. 4.2).

Please note that the observed trends are also retained at higher temperatures, as can be seen from the estimated thermal conductivities shown in Fig. 4.8 at the Debye temperature (430 K) and at 500 K. At these temperatures, pristine Mg_2Si features a thermal conductivity of 7.76 W/mK and 6.68 W/mK, which results in a parametrical mean free path Λ of 73.5Å and 62.4Å, respectively. This is not too surprising, given that the mode specific heat $c_s(\mathbf{q})$, i.e., the only temperature dependent parameter entering the CMFP calculation beside the defect-independent mean free path Λ, becomes temperature independent in this high temperature limit.
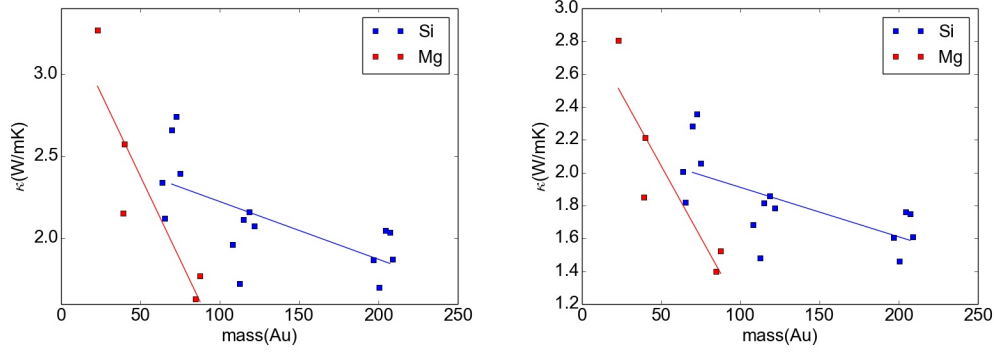
4.4.2 Constant Relaxation Time Approximation

In the *constant mean relaxation time* approximation (CMRT), the lattice thermal conductivity κ and the density of the thermal conductivity $\kappa_{dos}(\omega)$ were estimated by evaluating Eq. (2.91) for all doped magnesium silicides. The value for the required parameteric mean constant relaxation time τ was chosen to be 4.68 ps at 300K, i.e., the value for which CMRT and SMRTA calculations yield the exact same value of κ at 300K for pristine Mg_2Si (see Sec. 3.3). Essentially, this implies the assumption that the mean relaxation time changes only marginally upon doping, so that the value valid for the pristine material can be used for the doped structures as well.

In Fig. (4.9) the density of the thermal conductivity $\kappa_{dos}(\omega)$ calculated with the CMRT approximation for the doped structure in comparison with the one of the pristine Mg_2Si (both CMRT and full SMRTA) is shown. For all dopants a massive reduction of $\kappa_{dos}(\omega)$ above a
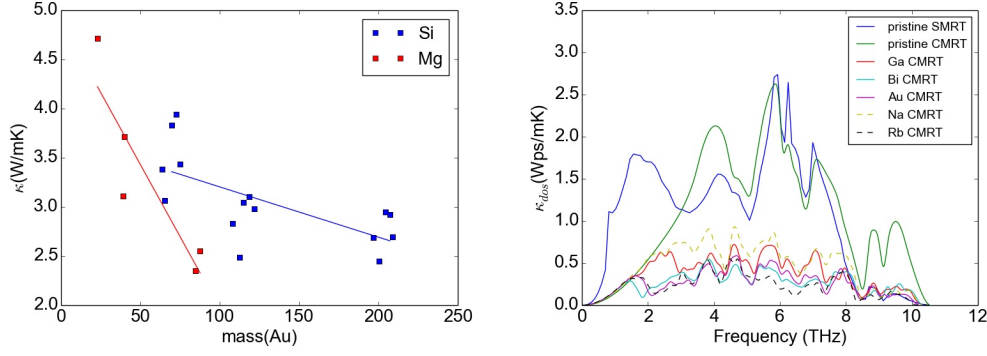
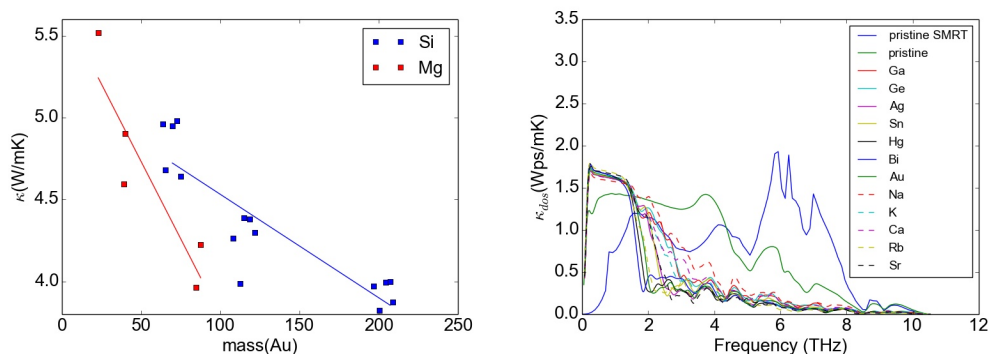**Figure 4.9:** Constant mean relaxation time approximation (CMRT) for substitutionally doped Mg$_2$Si: The left plot shows the density of the thermal conductivity $\kappa_{dos}(\omega)$ for selected substitutional doping on the Si (Ga, Bi, Au) and the Mg (Na,Rb) site. The right plot shows the estimated thermal conductivity at 300K plotted against the atomic mass of the dopant for all investigated substitutions.

Figure 4.10: Thermal conductivities estimated in the constant mean relaxation time approximation (CMRT) for substitutionally doped Mg$_2$Si as function of the dopants' mass (left: 430K, right: 500K)..

frequency above 2 THz is observed, which again agrees with the reduction observed for the averaged group velocity $\bar{v}(\omega)$ seen in Fig. 4.4 and 4.6. Just as before it is important to keep in mind that the contributions from low frequency modes are also underestimated using the CMRT, while the contribution from high frequency modes are overestimated (see Fig. 4.9). Given that the relative weight is shifted towards lower frequencies in the CMRT, this approximation suggests an even stronger decrease of the thermal conductivity upon doping, e.g., by a factor of 2.4 for Na and 4.73 for Rb. Qualitatively, the same trends (stronger reduction for heavy dopants and for substitution on the Mg site) as discussed before are observed. For the exact same reasons, these trends are again retained at higher temperatures, as shown in Fig. 4.10 for a temperature of 430K and 500K. At these temperatures, the thermal conductivity of pristine Mg$_2$Si (7.76 W/mK and 6.68 W/mK, respectively) leads to a constant mean relaxation time τ of 3.12 ps and 2.66 ps, respectively.

Figure 4.11: Slack's approximation for substitutionally doped Mg_2Si: The left plot shows the density of the thermal conductivity $\kappa_{dos}(\omega)$ for selected substitutional doping on the Si (Ga, Bi, Au) and the Mg (Na,Rb) site. The right plot shows the estimated thermal conductivity at 430K plotted against the atomic mass of the dopant for all investigated substitutions.

4.4.3 Slack's Method

Conversely to the CMFP and CMRT approximation, no constant scattering mechanism is assumed in Slack's method. Rather, the relaxation time scales analytically with $\omega_s^{-2}(\mathbf{q})$ and also depends on the temperature, as detailed in the discussion of Eq. (2.89). Still, Slack's method requires to estimate the parameter p. Here, it was chosen to be 0.06 ps^2, i.e., the value for which Slack's method exactly matches the thermal conductivity κ computed with the SMRT for pristine Mg_2Si at 430K. Again, this assumes that p does not depend significantly on the doping. In Fig. 4.11 the densities of the thermal conductivity $\kappa_{dos}(\omega)$ calculated with Slack's approximation for the doped magnesium silicides is shown. Compared to the CMFP and CMRT calculations, $\kappa_{dos}(\omega)$ is even more massively reduced for all frequencies above 2 THz, but slightly increases for frequencies below 2 THz. This is a result of the fact that the factor $\omega_s^{-2}(\mathbf{q})$ in the modeling of the relaxation times shifts the relative weight and importance of the modes to lower frequencies. Accordingly, the appearance of low-frequency modes in the spectra of doped compounds becomes notable in the $\kappa_{dos}(\omega)$ as well. Nonetheless, also Slack's method yields the exact same qualitative trends (stronger reduction for heavy dopants and for substitution on the Mg site) as discussed before. Given that Slack's method also accounts for the temperature dependence of the relaxation time, it also allows to estimate the thermal conductivity at different temperatures without changing the previously determined parameter p. Also in these case, the trends observed at 430K are retained at higher temperatures, as shown in Fig. 4.12.
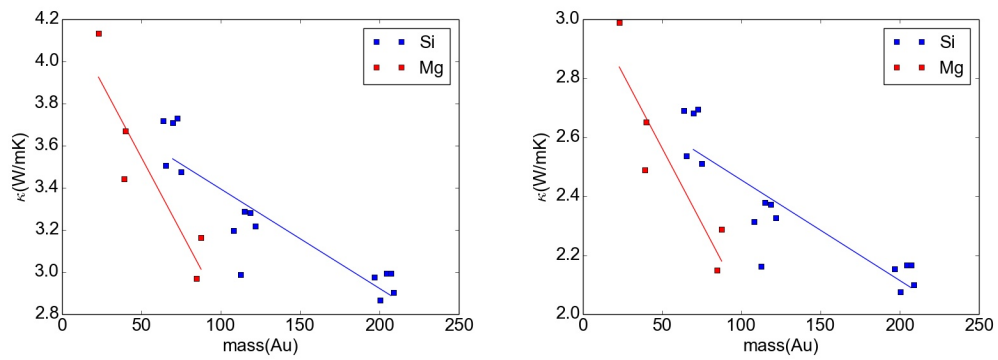
Figure 4.12: Thermal conductivities estimated in Slack's approximation for substitutionally doped Mg_2Si as function of the dopants' mass (left: 500K, right: 600K).

5 Outlook

As the previous chapters have shown, the existing semi-empirical approximations to rapidly estimate the thermal conductivity are capable of capturing some of the qualitative trends, e.g., the dependence of the thermal conductivity on the mass of the dopant. However, no reliable quantitative predictions appear to be possible: For instance, the thermal conductivity of Bi doped Mg_2Si is 3.6 (W/mK) in the CMFP, 1,9 (W/mK) in the CMRT, and 3.9 using Slack's method., in spite of the fact that the empirical parameters entering these approximations have been determined from high-level first-principles calculations of pristine Mg_2Si.

Recently, Madsen and coworkers [40] proposed a refinement to Slack's method, in which the empirical parameter p is determined from the Grüneisen parameter of the material. Although being a huge step forward, p is still frequency independent in this approach, so that the computed thermal conductivities would only be scaled by a constant factor. The qualitative, physical differences that appear in the density of the thermal conductivity $\kappa_{DOS}(\omega)$ when comparing Slack's method to the SMRTA (see Sec. 3.3) would, however, remain unchanged by this improvement.

Inspired by Madsen's work, we investigated if it is possible to extract more detailed information on the anharmonic interactions, i.e., the third order force constants $\Psi_{IJK}^{\alpha\beta\gamma}$, from the Grüneisen tensor $\gamma_s^{\mu\nu}(\mathbf{q})$ using the approaches proposed by Esfarjani [18]. Formally, this two quantities are related by

$$\gamma_s^{\mu\nu}(\mathbf{q}) = \sum_{IJK,\alpha\beta\gamma} \underbrace{\frac{-\epsilon_{I,s}^{*\alpha}(\mathbf{q})\epsilon_{J,s}^{\beta}(\mathbf{q})}{\sqrt{M_I M_J}2\omega_s^2(q)}\delta_{\mu\gamma}R_K^\nu e^{i\mathbf{q}\cdot(\mathbf{R}_J-\mathbf{R}_I)}}_{\Pi_{IJK,s}^{\alpha\beta\gamma,\mu\nu}(\mathbf{q})} \Psi_{IJK}^{\alpha\beta\gamma} . \tag{5.1}$$

already introduced and discussed for Eq. (2.74). Formally, inverting this relation requires to find a least square solution for this equation.

For this purpose, Eq. (5.1) is written in matrix form as

$$\sum_M \Pi_{\theta,M}\Psi_M = \gamma_\theta . \tag{5.2}$$

Here all the cartesian and atomic coordinates where mapped on one Voigt index using $\{\alpha\beta\gamma, IJK\} \to \{M\}$. The remaining indeces where also mapped on a different Voigt index using $\{\mathbf{q}, s, \mu, \nu\} \to \{\theta\}$. Both permutation symmetry and translational invariance were

imposed on the system to reduce the dimensionality of the problem. For the latter step, the following relation for the atomic position $\mathbf{R}$ is exploited:

$$\tilde{\mathbf{R}} = \mathbf{R} + \mathbf{T} \ . \tag{5.3}$$

Here, $\mathbf{T}$ is a translation vector of the system, as introduced in Sec. 2.1.3. In the practical implementation, these vectors were computed using the *spglib* package as included in *phonopy* [25]. However, no point group symmetry was exploited in the developed implementation, yet, due to time constrictions.

The "fitting" procedure itself was performed by pseudo-inverting Eq. (5.2) using a *singular value decomposition* (SVD) as implemented in the least square fitting procedure of the *numpy* [59] library. Essentially, this algorithm determines the minimum of the following equation

$$S(\mathbf{\Psi}) = \sum_\theta |\gamma_\theta - \sum_M \Pi_{\theta,M} \Psi_M|^2 \tag{5.4}$$

with respect to $\mathbf{\Psi}$ using a SVD.

In a first step, the outcome of such a fitting procedure was analyzed for CuCl in a $(1 \times 1 \times 1)$ cubic supercell. In this case, the third order force constants $\Psi_{IJK}^{\alpha\beta\gamma}$ were first computed using *phono3py*, as discussed in Sec. 3.2.1. The Grüneisen parameters were then computed using the $\Psi_{IJK}^{\alpha\beta\gamma}$ matrix elements and fed to the fitting algorithm. The $\Psi_{IJK}^{\alpha\beta\gamma}$ "reconstructed" by this means are compared to the original third order force constants $\Psi_{IJK}^{\alpha\beta\gamma}$ in Fig. 5.1. Generally, the reconstructed force constants reproduce the behaviour of the original force constants. Still, some numerical noise is present: Mostly, this arises from the fact that no point group symmetry is imposed. Also, the most strong deviations are observed for the diagonal elements $\Psi_{III}^{\alpha\alpha\alpha}$ at -10/12 eV/Å^3, in which the deviations accumulate due to the imposed acoustic sum rule:

$$\Psi_{III}^{\alpha\beta\gamma} = -\sum_K \Psi_{IIK}^{\alpha\beta\gamma} \tag{5.5}$$

Despite the relatively good agreement, the "reproduced" third order force constants $\Psi_{IJK}^{\alpha\beta\gamma}$ shown in Fig. 5.1 yield a thermal conductivity that is 34% too low (0.27 W/mK at 300 K instead of 0.41 W/mK). Again, this can be traced back to the omission of point group symmetry in the current implementation: Entries in $\Psi_{IJK}^{\alpha\beta\gamma}$ that should be equal and then cancel out in the computation of κ are not equal due to the numerical noise and thus add up to noticeable reduction in lifetime. Still, the results are very encouraging, even at this very crude stage of development, given that the proposed technique is fully parameter-free: In a nutshell, the developed approach allows to extract third order force constants $\Psi_{IJK}^{\alpha\beta\gamma}$ from Grüneisen parameters γ. Given that the latter can computed from the quasi-harmonic approximation (see Sec. 2.2.3), this results into orders of magnitude lower computational cost than the one required to determine third order force constants $\Psi_{IJK}^{\alpha\beta\gamma}$ via finite differences or perturbation theory. To fully test, analyze, and exploit the potential of the proposed approach more implementation work is required: Especially,
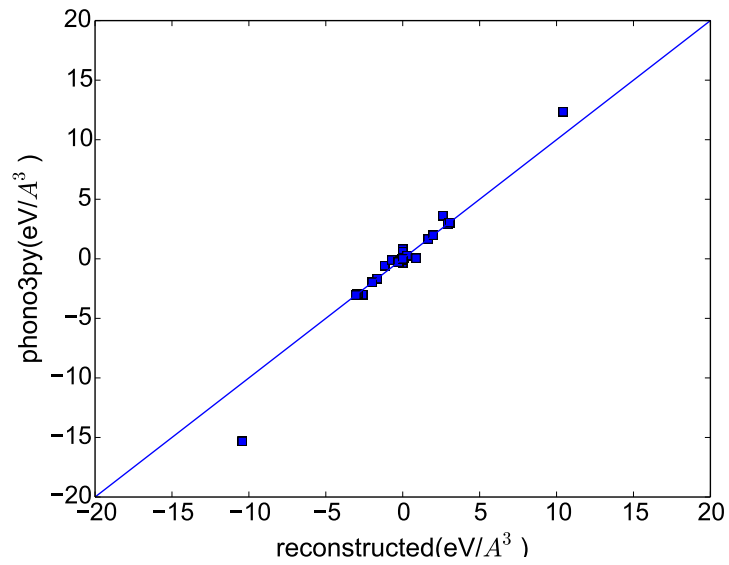
Figure 5.1: Third order force constants calculated with *phono3py* versus reconstructed third order force constants for CuCl. Using a PBEsol functional in a $(1 \times 1 \times 1)$ cubic unit cell

CPU and memory bottlenecks that currently affect this proof-of-concept implementation need to be removed to male the technique applicable for productive calculate on a large scale.

6 Conclusion

After giving a concise introduction into the fundamental physics underlying this thesis, we investigated the fundamental properties of Mg_2Si, and found that our results are in good agreement with previously conducted experimental and theoretical works. Particular focus was laid on the harmonic and anharmonic vibrational properties of Mg_2Si. To better frame the discussion, we compared Mg_2Si to Si and CuCl, two materials which are known for their harmonic/anharmonic behavior. This enabled us to perform an in depth analysis of three different semi-empirical models used to estimate the vibrational thermal conductivity, namely the *constant mean free path* approximation, the *constant mean relaxation time*, and a empirical lifetime suggested by Slack. By analysing their performance in comparison with the well established single mode relaxation time approximation for Mg_2Si, Si, and CuCl. We found that, while these models are not accurate enough to yield quantitatively good results, they indeed are capable of predicting qualitatively correct trends for doping. Using these models, we found that the thermal conductivity of Mg_2Si reduces massively upon doping. Additionally we found that heavier dopants are generally more effective in lowering the thermal conductivity. Also substitutions on the Mg-site are more effective than substitutions on the Si site. Finally an outlook was given for a promising parameter free method to predict the third order force constants, typically used to calculate anharmonic quantities such as the thermal conductivity.

6.1 Acknowledgement

Ich möchte mich zuallererst bei meiner Familie und meinen Freunden für die Unterstützung bedanken die sie mir das ganze leben über haben zukommen lassen.
Ausserdem gilt mein Dank Prof. Matthias Scheffler und Prof. Andreas Knorr ohne die diese Arbeit nicht möglich gewesen wäre.
Ausserdem gilt mein dank auch Luca Ghiringhelli der co Betreuer meiner Arbeit war.
Ein ganz besonderer Dank geht aber an Christian Carbogno der immer auf jede Frage die ich hatte eine Antwort wusste.

Bibliography

[1] A. G. Evans, D. R. Clarke, and C. G. Levi, J. Eur. Ceram. Soc. 28, 1405 (2008).

[2] B.Orr, et.al., Appl. Therm. Eng., 101 490-495 (2016)

[3] R. M. Martin, Electronic Structure Basic Theory and Practical Methods, Cambridge University Press, Cambridge (2010)

[4] F. Jensen, Introduction to Computational Chemistry, Wiley (2017)

[5] P. Hohenberg and W. Kohn. Phys. Rev. 136, B864 (1964)

[6] R.Parr and W. Yang, Density Functional Theory of Atoms and Molecules, Oxfort University Press, Oxfort (1989)

[7] W. Kohn and L. J. Sham, Phys. Rev. 140, A1133 (1965)

[8] Yan Alexander Wang, Niranjan Govind, and Emily A. Carter Phys. Rev. B 60, 16350 (1999)

[9] P. J. Perdew, et.al., Phys. Rev. Lett, 77 ,18 (1996)

[10] P. J. Perdew, et.al., Phys. Rev. Lett, 100 ,136407 (2008)

[11] Aron J. Cohen, et,.al., Science 321, 5890, 792-794 (2008);

[12] P. J. Perdew, et.al., J. Chem. Phys., 105, 9982 (1996)

[13] J. Heyd, G. E. Scuseria, and M. Ernzerhof, J. Chem. Phys. 118, 8207 (2003).

[14] P. Pulay, Mol. Phys. 17 (1969) 197

[15] Gonze and J.-P. Vigneron, Phys. Rev. B 49, 13 120 (1989)

[16] R. P. Feynman, Phys. Rev. 56, 340 (1939)

[17] D. Frenkel, B. Smit, Understading Molecular Simulation From Algorithms to Applications, Academic Press, New York, (2002)

[18] K. Esfarjani and H. T. Stokes, Phys. Rev. B, 77, 144112 (2008)

[19] O. Hermann and I. A. Abrikosov, Phys. Rev. B 88 , 144301 (2013)

[20] S. Biernacki and M. Scheffler, Phys. Rev. Lett. 63, 290 (1989)

Bibliography

[21] S. Baroni, et.al., Rev. Mod. Phys. 73, 515 (2001)

[22] X. Gonze and J.-P. Vigneron, Phys. Rev. B 39, 13120 (1989)

[23] A. Cepellotti, et.al., Nat. Commun., 6, 6400 (2015)

[24] K. Parlinski, Z.Q. Li, Y. Kawazoe, Phys. Rev. Lett. 78 (1997)

[25] A. Togo and I. Tanaka, Scr. Mater., 108, 1-5 (2015)

[26] A. Togo, L. Chaput, and I. Tanaka, Phys. Rev. B, 91, 094306 (2015)

[27] J. Garg, et.al., Phys. Rev. Lett. 106, 045901 (2011)

[28] A. Chernatynskiy and S. R. Phillpot, Phys. Rev. B 82, 134301 (2010).

[29] C. Carbogno, et.al., arXiv:1608.06917 (2016)

[30] Kubo, M. Yokota, and S. Nakajima, J. Phys. Soc. Japan 12, 1203 (1957).

[31] Fei Zhou, et.al.,Phys. Rev. Lett. 113, 185501 (2014)

[32] D. C. Wallace, Thermodynamics of Crystals, Dover Publishing Inc., New York (1972)

[33] V. Blum, et.al., Comput. Phys. Commun. 180, 2175-2196 (2009)

[34] M.Akasaka, et. al., J. Cryst. Growth, 304, 196-201 (2007)

[35] N. W. Ashcroft, N. D. Mermin, Solid State Physics, Saunders College Publishing, New York, (1976)

[36] G. P. Srivastava, The Physics of Phonons, Adam Hilger, Bristol, (1990)

[37] L. Chaput, Phys. Rev. Lett. 110, 265506 (2013)

[38] A. A. Maradudin and A. E. Fein, Phys. Rev.128, 2589 (1962)

[39] G. A. Slack and S. Galginaitis, Phys. Rev.133,A253 (1964)

[40] L. Bjerg, et.al., Phys. Rev.B,89,024304(2014)

[41] Y.He and G. Galli, Nano Lett., 14, 2920 (2014)

[42] O. Maelung, U. Rössler, O. Schulz,Non-Tetrahedrally Bonded Elements and Binary Compounds I,Springer Berlin Heidelberg, Berlin

[43] E. Anastassakis and J. P. Hawranek, Phys. Rev. B 5, 4003 (1972)

[44] J. de Boor, et. al., J Mater Sci, 49: 3196, (2014)

[45] Gaosheng Fu, et.al, J. Appl. Phys., 114, 144905 (2013)

[46] F. Vazquez, R.A. Forman, and M. Cardona, Phys. Rev.176, 905 (1968)

[47] B. Arnaud and M. Alouani, Phys. Rev. B 64, 033202 (2001)

[48] J. Behler, B. Delley, S. Lorenz, K. Reuter, and M. Scheffler, Phys. Rev. Lett. 94, 036104 (2005).

[49] C. Carbogno, J. Behler, A. Groß, and K. Reuter, Phys. Rev. Lett. 101, 096104 (2008).

[50] F. Birch, Phys Rev 71, 809 (1947).;

[51] F. Murnaghan, Proc. Natl. Acad. Sci. 30, 244 (1944).

[52] A. M. Wodtke, J. C. Tully, and D. J. Auerbach, International Reviews in Physical Chemistry 23, 513 (2004).

[53] N. Shenvi, S. Roy, and J. Tully, Science 326, 829 (2009).

[54] M. Akasaka, et.al., J. Cryst. Growth 304, 196 (2007).

[55] Q. Zhang J. Alloys Compd. 464, 1–2, 9–12, (2008),9–12

[56] J. De Boor, et. al., J. Alloys Compd., 632 348-353 (2015)

[57] S.Fiameni, et.al., J. Solid State Chem., 193 142-146 (2012)

[58] P. Zwolenski, J. Tobola and S. Kaprzyk,J. Electron.Mater.,40, 889-897 (2011)

[59] Stéfan van der Walt, S. Chris Colbert and Gaël Varoquaux, COMPUT SCI ENG, 13, 22-30 (2011)

7 Appendix

Tab. 7.1 shows the computational settings choosen for Si and CuCl

Fig. 7.1 shows the convergence of the lattice constant $a_0(\text{Å})$ and the bulk modulus $B_0(\text{eV/Å}^3)$ with the **k**-point grid. The lattice constant as well as the bulk modulus converge rapidly with the number of **k**-points. However to ensure an optimal convergence a dense $(12 \times 12 \times 12)$ **k**-grid was chosen.

Fig. 7.2 shows the convergence of the lattice constant $a_0(\text{Å})$ and the bulk modulus $B_0(\text{eV/Å}^3)$ with the chosen *FHI-aims* basis functions. Here Si1Mg1 means Si first tier and Mg first tier. The choice of the basis set influences the lattice constant $a_0(\text{Å})$ only in the milli angström range. Also the bulk modulus $B_0\text{Å}$ changes only minimally with the number of basis functions. However to ensure However to ensure results with a small error margin, while also allowing for a efficient computation silicon first tier and magnesium second tier was chosen.

Fig. 7.3 shows the convergence of the lattice constant $a_0(\text{Å})$ and the bulk modulus $B_0(\text{eV/Å}^3)$ with the chosen *FHI-aims* integration grids. The lattice constant $a_0(\text{Å})$ depends minimally on the chosen integration grid, the bulk modoulus $B_0(\text{eV/Å}^3)$ however depends stronger on the chosen integration grid. To ensure good results a tight integration grid was chosen.

| Settings	CuCl	Si
k-point grid	$(6 \times 6 \times 6)$	$(6 \times 6 \times 6)$
Tiers	Cu 2 Cl 2	Si 2
Integration-grid	tight	tight
Supercell	cubic $(2 \times 2 \times 2)$	cubic $(2 \times 2 \times 2)$

Table 7.1: Computational Settings for CuCl (zincblend) and Si (diamond).
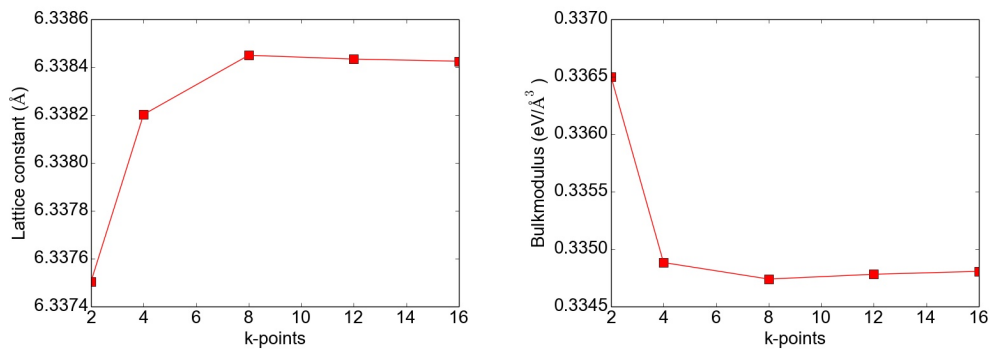
Figure 7.1: Lattice constant (left) and bulk modulus (right) of Mg$_2$Si using PBEsol and light settings plotted against the number of **k**-points. As can be seen the influence of the **k**-point grid on the lattice constant is in the m range also the Bulkomulus changes minimally and can be regarded as converged at a $(4 \times 4 \times 4)$ **k**-point grid. However to minimize the total error of the calculations a dense $(12 \times 12 \times 12)$ **k**-point grid was chosen.
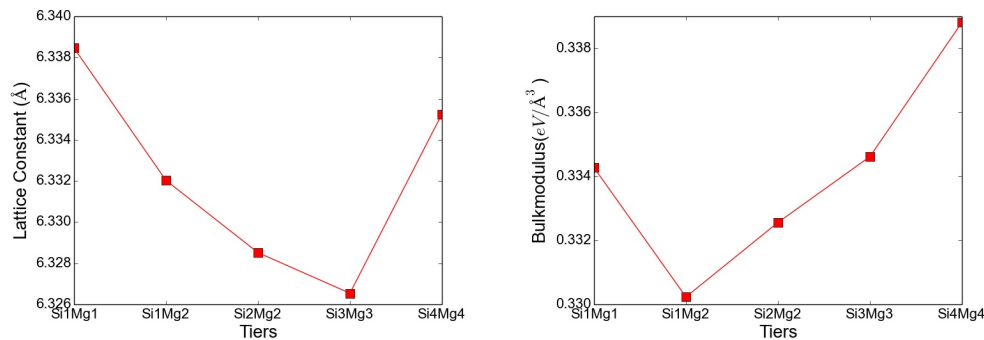
Figure 7.2: Lattice constant (left) and bulkmodulus (right) of Mg$_2$Si using PBEsol and light settings and a $(12 \times 12 \times 12)$ **k**-point grid plotted against the respective basisfunction tiers. Here Si1Mg1 means Silicon first tier and Magnesium first tier. The influence of the chosen basis functions one the lattice constant is the mÅ range. The bulk modulus also changes only minimally with the number of basis functions. However to ensure results with a small error margin, while also allowing for a efficient computation silicon first tier and magnesium second tier was chosen.
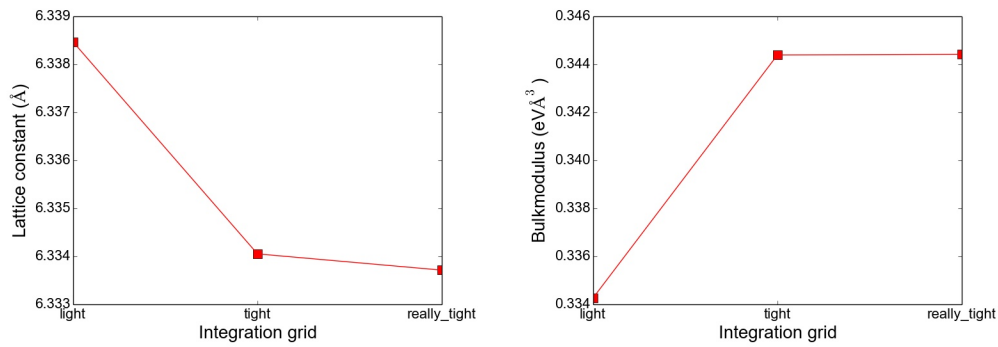
Figure 7.3: Latticeconstant (left) and Bulkmodulus (right) of Mg_2Si using PBEsol a $(12 \times 12 \times 12)$ **k**-point grid and first tiers plotted against different *FHI-aims* integration grids. The lattice constant $a_0(\text{Å})$ depends minimally on the chosen integration grid, the bulk modoulus $B_0(\text{eV}/\text{Å}^3)$ however depends stronger on the chosen integration grid. To ensure good results a tight integration grid was chosen